IRAQI JOURNAL OF APPLIED PHYSICS

The *Iraqi Journal of Applied Physics (IJAP)* is a peer reviewed journal of high quality devoted to the publication of original research papers from applied physics and their broad range of applications. IJAP publishes quality original research papers, comprehensive review articles, survey articles, book reviews, dissertation abstracts in physics and its applications in the broadest sense. It is intended that the journal may act as an interdisciplinary forum for Physics and its applications. Innovative applications and material that brings together diverse areas of Physics are particularly welcome. Review articles in selected areas are published from time to time. It aims to disseminate knowledge; provide a learned reference in the field; and establish channels of communication between academic and research experts, policy makers and executives in industry, commerce and investment institutions. IJAP is a quarterly specialized periodical dedicated to publishing original papers, letters and reviews in: Applied & Nonlinear Optics, Applied Mechanics & Thermodynamics, Digital & Optical Communications, Electronic Materials & Devices, Laser Physics & Applications, Plasma Physics & Applications, Quantum Physics & Spectroscopy, Semiconductors & Optoelectronics, and Solid State Physics & Applications

SPONSORED AND PUBLISHED BY
THE IRAQI SOCIETY FOR ALTERNATIVE AND RENEWABLE ENERGY SOURCES & TECHNIQUES (I.S.A.R.E.S.T.)

IRAQI JOURNAL OF APPLIED PHYSICS
" INSTRUCTIONS TO AUTHORS "

CONTRIBUTIONS

Contributions to be published in this journal should be original research works, i.e., those not already published or submitted for publication elsewhere, individual papers or letters to editor.

SUBMISSION OF MANUSCRIPTS

Manuscripts should be submitted to the editor at the mailing address:

Iraqi Journal of Applied Physics
Editorial Board
P. O. Box 55259, Baghdad 12001, IRAQ, submission@ijap.org , editor@ijap.org

MANUSCRIPTS

Two hard copies with soft copy on a compact disc (CD) should be submitted to Editor in the following configuration:

- Double-spaced one-side A4 size with 2.5 cm margins of all sides
- Times New Roman font (16pt bold for title, 14pt bold for names, 12pt bold for headings, 12pt regular for text)
- Letters should not exceed 10 pages, papers should not exceed 20 pages and reviews are up to author.
- Manuscripts presented in English only are accepted.
- English abstract not exceed 150 words
- 4 keywords (at least) should be maintained on (PACS preferred)
- Author(s) should express all quantities in SI units
- Equations should be written in equation form (*italic* and symbolic)
- Figures and Tables should be separated from text
- Figures and diagrams can be submitted in colors for assessment and they will be returned to authors after provide printable copies
- Charts should be indicated by the software used for
- Only original or high-resolution scanner photos are accepted
- For electronic submission, articles should be formatted with MS-Word software.

AUTHOR NAMES AND AFFILIATIONS

It is IJAP policy that all those who have participated significantly in the technical aspects of a paper be recognized as co-authors or cited in the acknowledgments. In the case of a paper with more than one author, correspondence concerning the paper will be sent to the first author unless staff is advised otherwise.

Author name should consist of first name, middle initial, last name. The author affiliation should consist of the following, as applicable, in the order noted:

- Company or college (with department name or company division)
- Postal address
- City, state, zip code
- Country name
- Telephone, and e-mail

REFERENCES

The references should be brought at the end of the article, and numbered in the order of their appearance in the paper. The reference list should be cited in accordance with the following examples:

[1] X. Ning and M.R. Lovell, "On the Sliding Friction Characteristics of Unidirectional Continuous FRP Composites", *ASME J. Tribol.*, 124(1) (2002) 5-13.
[2] M. Barnes, "Stresses in Solenoids", *J. Appl. Phys.*, 48(5) (2001) 2000–2008.
[3] J. Jones, "Contact Mechanics", Cambridge University Press (Cambridge, UK) (2000), Ch.6, p.56.
[4] Y. Lee, S.A. Korpela and R. Horne, "Structure of Multi-Cellular Natural Convection in a Tall Vertical Annulus", Proc. 7th International Heat Transfer Conference, U. Grigul et al., eds., Hemisphere (Washington DC), 2 (1982) 221–226.
[5] M. Hashish, "Waterjet Technology Development", High Pressure Technology, PVP-Vol. 406 (2000), 135-140.
[6] D.W. Watson, "Thermodynamic Analysis", ASME Paper No. 97-GT-288 (1997).
[7] C.Y. Tung, "Evaporative Heat Transfer in the Contact Line of a Mixture", Ph.D. thesis, Rensselaer Polytechnic Institute, Troy, NY (1982).

PROOFS

Authors will receive proofs of papers and are requested to return one corrected hard copy with a WORD copy on a compact disc (CD). New materials inserted in the original text without Editor permission may cause rejection of paper.

COPYRIGHT FORM

Author(s) will be asked to transfer copyrights of the article to the Journal soon after acceptance of it. This will ensure the widest possible dissemination of information.

OFFPRINTS

Authors will receive offprints free of charge and any additional offprints can be ordered.

SUBSCRIPTION AND ORDERS

Annual fees (4 issues per year) of subscription are:

- 50 US$ for individuals inside Iraq.
- 100 US$ for establishments inside Iraq.
- 100 US$ for individuals abroad.
- 200 US$ for establishments abroad.

Fees are reduced by 25% for I.S.A.R.E.S.T. members. Orders of issues can be submitted by contacting the editor-in-chief or editorial office at **subscription@ijap.org** to maintain the address of issue delivery and payment way.

Luminescent Plates Doped with Stilbene 420 Dye for Enhanced Silicon Solar Cell Performance: Down-Conversion

Suma H. Al Shaikh Hussin

Department of Physics,
College of Science for Women,
University of Baghdad,
Baghdad, Iraq

The luminescent plates down-converting (DC) have the potential to generate more than one low-energy photon for every incident high-energy photon by adding laser dyes that have the ability to absorb high-energy photons that act in ultra-violet region such as stilbene 420 dye and emit low-energy photons in the visible region and so enhanced conversion efficiency (η) from 2.88% to 3.82% and so achieved an increase in conversion efficiency (Δη) up to 32.69% .That means the (DC) convert the high-energy solar photons to multiple photons having energy grater than of silicon band gap .The luminescent plates have been prepared by doping the epoxy resin with stilbene 420 dye that is dissolved in methanol in concentration of 1.8×10^{-3} mol/L and different thickness. The optical properties of luminescent plates in silicon solar cell was studied and discussed in door and out door showing an increase in conversion efficiency with the increase in luminescent plates thickness.

Keywords: Down-conversion, Stilbene 420 dye, Solar cell, Optical properties
Received: 12 October, **Revised**: 22 November, **Accepted**: 01 December 2010

1. Introduction

Conventional solar cells only effectively convert photons of energy close to the semiconductor band gap E_g as a result of the mismatch between the incident solar spectrum and the spectral absorption properties of the material. Photons with energy E_{ph} smaller than the band gap are not absorbed. Photons with energy E_{ph} larger than the band gap are absorbed, but the excess energy (E_{ph}-E_g) is not used effectively due to thermalisation of the electrons [1].

There are three photon conversion processes of interest, namely, down-shifting, down-conversion (DC) and up conversion (UC). These processes are illustrated schematically in Fig. (1). Of the three photon conversion processes, both DC and UC are of particular importance since they are both multiphoton processes that are able to minimize thermalisation and sub-band gap losses, respectively, from PV device [2].

The first publications on LSCs first appeared in the late 1970s [3] and the technology was studied intensely through the early 1980s until limitations of fluorescent organic dyes hindered further development [4].

The operation of an LSC is as follows in Fig. (2): (i) Light is absorbed by luminescent chromophores embedded within a waveguide. (ii) The chromophores re-emit a photon of lower energy, and some portion of the emitted light is confined in the waveguide by total internal reflection. (iii) The trapped light is guided to a solar cell [5].

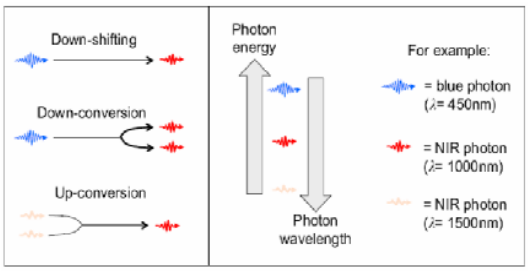

Fig. (1) Photon luminescent conversion processes

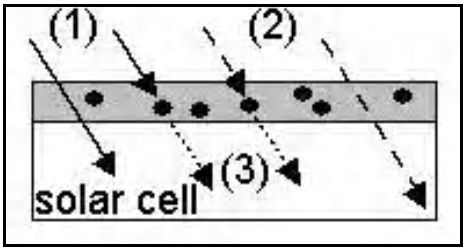

Fig. (2) Schematic drawing of the studied configuration. A plastic epoxy layer containing S-420 dye is applied on top of a solar cell

A red shift of the photon flux against the incident spectrum is often observed e.g. in Photoluminescence experiments, which is referred to as the Stokes-shift. Rather then just shifting the energy of incident photons it is also possible that incident high energy photons are transformed by a material into two or more lower- energy photons, which we will refer to here as down-conversion. Figure 3 shows a device schematic of a solar cell in combination with a down-converter.

The down converter ideally transforms incident photons with energies exceeding n-times the band-gap energy of the solar cell material into n lower energy photons, which can then be used for the generation of n eh-pairs inside the solar cell. Down-conversion thus represents a method for multiple eh-pair generation per incident high-energy photon and can be used to reduce the thermalisation losses. Because the absorption of high-energy photons in the solar cell must be avoided, the converter must be located on the front surface for semiconductor solar cells, as shown in Fig. (3) [6].

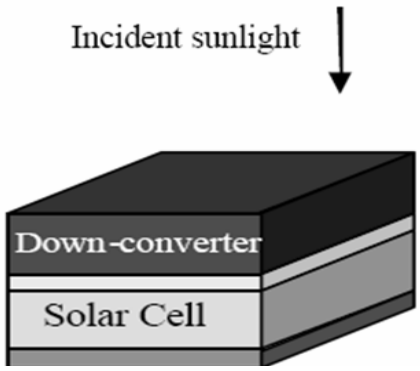

Fig. (3) Device schematic of a solar cell in combination with a down-converter

2. Experiment

The DC plates have been made in the lab in different thickness and suitable dimension to the Si-solar cell that is used. The transparent epoxy resin matrix are doped with stilbene 420 laser dye (S-420) that is dissolved in methanol in concentration of 1.8×10^{-3}mol/L; and the purchased dye have the following characteristic [7]:

Chemical name: $C_{28}H_{20}O_6S_2Na_2$
Molecular weight: 568.74
Appearance: yellow powder
Wavelength (nm): UV
Molar absorptivity (in methanol): (270-400)nm
Peak absorption: 350 (nm)
Fluorescence rang: (415-465)nm
Peak fluorescence: 430 (nm)

Structure of stilbene 420 dye is shown in Fig. (4) and the epoxy or polyepoxide is a thermosetting polymer formed from reaction of an epoxide "resin" with polyamine "hardener". Epoxy has a wide range of applications, including fiber-reinforced plastic materials and general purpose adhesives.

Epoxy is a copolymer; that is, it is formed from two different chemicals. These are referred to as the "resin" and the "hardener". The resin consists of monomers or short chain polymers with an epoxide group at either end shown in Fig. (5). Most common epoxy resins are produced from a reaction between epichlorohydrin and bisphenol-A, though the latter may be replaced by similar chemicals. The hardener consists of polyamine monomers, for example Triethylenetetramine (TETA).

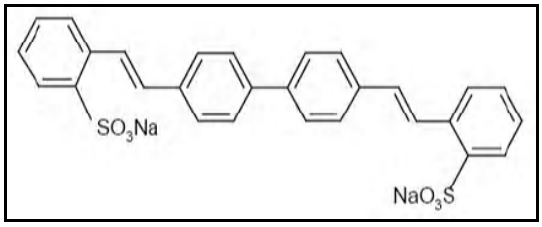

Fig. (4) The structure of stilbene 420 dye

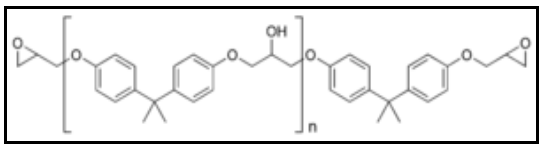

Fig. (5) Structure of unmodified epoxy prepolymer. n denotes the number of polymerized subunits and is in the range from 0 to about 25

When these compounds are mixed together, the amine groups react with the epoxide groups to form a covalent bond. Each NH group can react with an epoxide group, so that the resulting polymer is heavily crosslinked, and is thus rigid and strong [8]. The DC plates are prepared in the lab by incorporating the S-420 dye in transparent epoxy as base substance.

The used solar cell is a monocrystalline silicon solar cell type (C2100). It is circular shaped and have a diameter of (10 cm), thickness (0.5±0.15)mm and area (78.5±1.5)cm^2. Most solar cell parameters can be obtained from simple IV measurements. Figure (6) shows the IV characteristics of a typical solar cell under forward bias and illumination. The short circuit current (I_{sc}) is the current through the solar cell when the voltage across the solar cell is zero. The open circuit voltage (V_{oc}) is the voltage across the solar cell when the current through the solar cell is zero and it is the maximum voltage available from the solar cell. The maximum power point (P_{max}) is the condition under which the solar cell generates its maximum power; the current and voltage in this condition are defined as I_{max} and V_{max}, respectively. The fill factor (FF)

and the conversion efficiency (η) are metrics used to characterize the performance of the solar cell. The fill factor is defined as the ratio of P_{max} divided by the product of V_{oc} and I_{sc}.

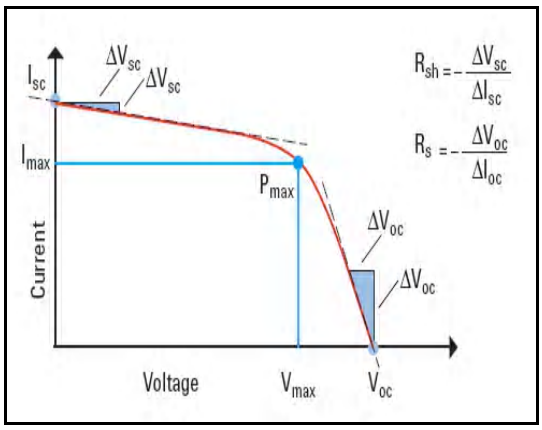

Fig. (6) Typical IV forward bias characteristics of a solar cell

The conversion efficiency is defined as the ratio of P_{max} to the product of the input light irradiance (E) and the solar cell surface area (A_c) [9]:

$$FF = \frac{P_{max}}{V_{oc} I_{sc}} \quad (1)$$

$$\eta = \frac{P_{max}}{E \times A_c} \times 100\% = \frac{V_{oc} \times I_{sc} \times FF}{E \times A_c} \times 100\% \quad (2)$$

Enhancement in the efficiency by using down-conversion luminescent plate is given as:

$$\Delta\eta = \frac{(\eta\%)_{DC} - (\eta\%)_{bare}}{(\eta\%)_{bare}} \times 100\% \quad (3)$$

where $(\eta\%)_{DC}$ is the conversion efficiency by using down-conversion luminescent plate, and $(\eta\%)_{bare}$ is the conversion efficiency for bare solar cell

Although there are a variety of methods to estimate R_{sh} and R_s, one of the most straightforward techniques is to measure the slope of I-V characteristics as shown in Fig. (7).

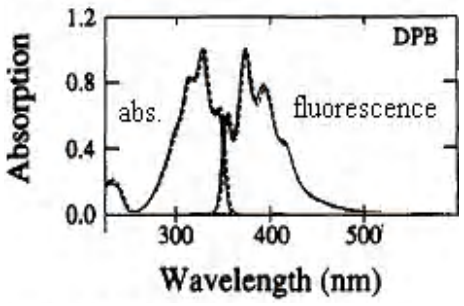

Fig. (7) The absorption & the fluorescence spectrum to the S-420 dye dissolved in methanol [13]

Unfortunately, the value of R_s calculated using this method tends to be proportional to but larger than the actual value [10]. The parameter of solar cell are measured and calculated first in the lab (indoor) and then in the direct sunlight (outdoor).

Optical properties of the down-conversion luminescent plate, absorbance (A), transmittance (T), reflectance (R) and refractive index (n) were studied with epoxy doped with stilbene 420 dye that are transparent yellow plates, to show its importance in determine the range of ability to use the down-conversion luminescent plate in optical applied of solar cell.

The equations of A, T and R are [11,12]:

$$A = \log_{10} \frac{1}{T} \quad (4)$$

$$R = 1 - A - T \quad (5)$$

$$n = \left[\left(\frac{4R}{(R-1)^2} \right) - (k_o^2) \right]^{1/2} - \frac{R+1}{R-1} \quad (6)$$

where k is the extinction coefficient

The stilbene 420 (S-420) dye laser has strong absorbance in ultra-violet region to convert higher incident photon energy to visible region and also it has large cross section as shown in figure 7 and that is what solar cells needs [13].

3. Result and Discussion

This study investigates a method of increasing the performance of Si-solar cells by placing a luminescent medium on the top the cell. The conversion efficiency (η) of the bare Si-solar cell that use in this study is calculated according to Eq. (2) and it's shown in Fig. (8) and η are the measure of indoor and outdoor conversion efficiency and equal to $\eta_{(in)}$=2.88% and $\eta_{(out)}$=1.53%, respectively.

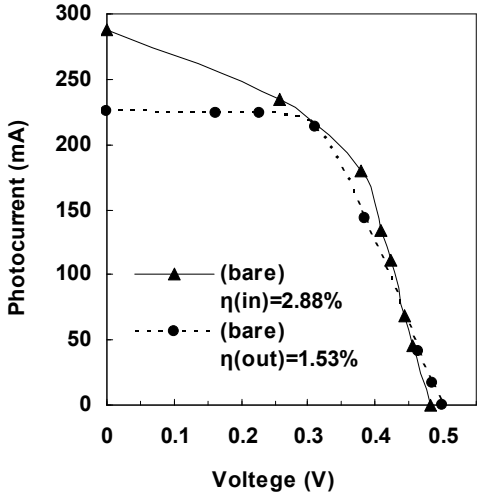

Fig. (8) The conversion efficiency of the bare Si-solar cell indoor and outdoor ($\eta_{(in)\%}$, $\eta_{(out)\%}$), respectively.

The conversion efficiency $(\eta)_{DC}$ with the use of DC plates at different thicknesses (d) about (1.5,2,2.85,3.3,4)mm is calculated according to

Eq. (2) and compared with $(\eta)_{bare}$ Si-solar cell to find the increasing in conversion efficiency ($\Delta\eta$) that calculated by Eq. (3) and both η and $\Delta\eta$ are measured indoor and outdoor, as shown in Fig. (9).

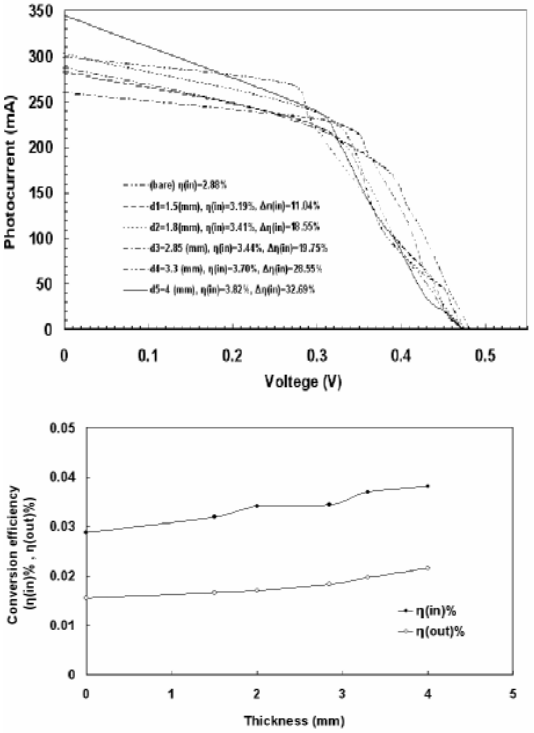

Fig (9) The comparison between $(\eta)_{bare}$ Si solar cell and $(\eta)_{DC}$ with the use of DC plates and enhancement of conversion efficiency ($\Delta\eta$) in different thicknesses

The DC plate of 4mm thickness gives the best conversion efficiency in comparison with other thicknesses of DC plates used in this study as $\eta_{(DC)}$=3.82% and $\Delta\eta$=32.69% at d=4mm. The prefabricated cells used here have low conversion efficiency. The prepared DC plates can be used with both high and low conversion efficiency solar cells, and in both states the DC plates improves the performance of the solar cells [14].

The absorbance and transmittance spectrum are measured by UV-VIS spectrophotometer from company Shimadzu-Japan have wavelength rang of (200-1100)nm. Then the fluorescent spectrum measured by spectrofluorometer (type SL174) in the wavelength range of (200-900)nm.

The spectra of reflectance (R) and refractive index (n) are calculated according to equations (5) and (6), respectively.

The optical properties for DC plates are studied to find the properties of these plates. Figure (10) shows the absorption spectrum of base material (epoxy resin) and DC plates. The peaks (1) refer to absorbance of pure epoxy resin at wavelength of 340nm at different thicknesses and peaks (2) point to the absorbance of the DC plates at wavelength of 380nm. When the thicknesses of plate increases, then the absorbance increases too.

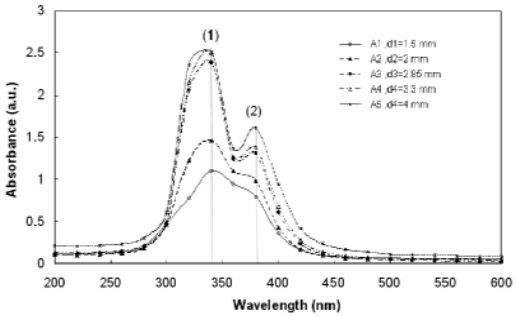

Fig. (10) Absorption spectrum (1) of epoxy resin, and (2) the DC plates of different thicknesses

The spectra of fluorescent of these plates involve the DC plate at d=4mm, as shown in Fig. (11). Its peak of fluorescence is at wavelength of 422nm, and this wavelength is dependent to calculate the optical properties.

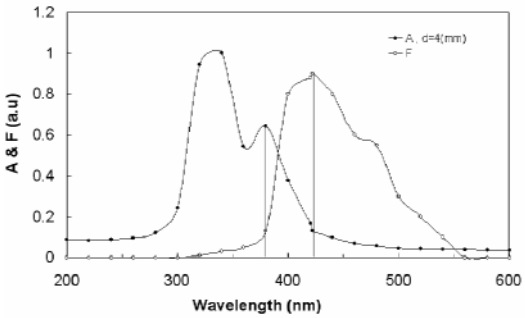

Fig. (11) The spectra of absorbance (A) and fluorescence (f) of DC plate at d=4mm and the Stoke shift ($\Delta\lambda$) of 42 (nm)

The absorbance spectrum is shifted towards higher wavelengths (red shift) and it is called Stoke shift ($\Delta\nu$), which refers to the difference between the peaks of absorbance and fluorescence spectra [15], which is equal to $\Delta\eta$=42nm. The highest shift obtained from DC plates is given at DC plate of 4mm thickness and that plate represents the maximum thickness used in this study. When the thickness increases, the number of dye molecules are increased too [16] and this affects the operation of fluorescent because of the increasing in Stoke shift [17].

The spectrum of transmittance (T) of DC plates shown in Fig. (12) shows that minimum transmittance occurs at wavelengths within (320-380)nm. At wavelength range of (380-450)nm, the transmittance is ranging from 20% to 80% and the highest transmittance (90-99)% occurs at wavelength range of (450-1100)nm. When the thickness increases, then the transmittance decreases.

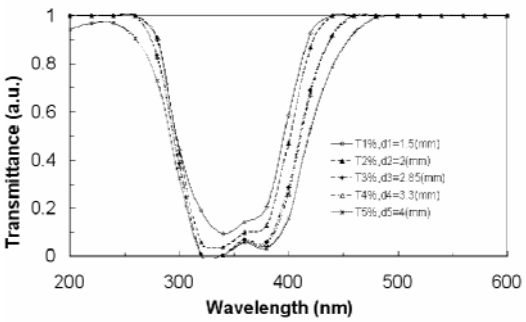

Fig. (12) The transmittance (T) spectrum of DC plates in different thicknesses (d)

The wavelength-dependent behavior of the reflectance (R) is shown in Fig. (13). The reflectance is found according to Eq. (5) and the maximum value of reflectance (20%) is obtained at wavelength range of (300-410)nm and it is 15% at active wavelength (422nm). The reflectance is decreased with increasing wavelength.

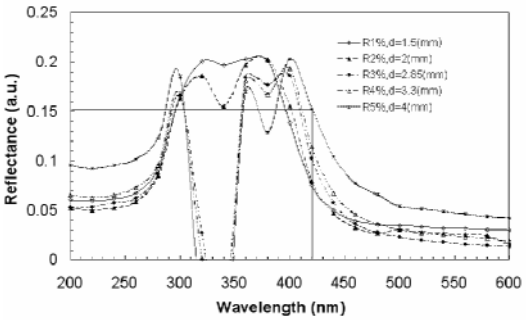

Fig. (13) The reflectance (R) of DC plates at different thicknesses (d)

The refractive index (n) is calculated according to Eq. (6) and shown in Fig. (14) at different thicknesses of DC plates. It is found to be 2.3 at wavelength of 422nm.

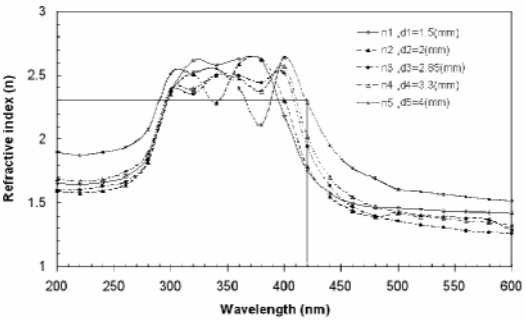

Fig. (14) Refractive index (n) of DC plates at different thicknesses (d)

4. Conclusion

There is an advantage to use higher photon energy at ultraviolet (UV) region to raise the conversion efficiency of silicon solar cells by using a laser dye that absorbs in UV region and re-emit in visible region, so it shifts the spectrum towards the higher response to the solar radiation by down-conversion photon energy. So, it improves the conversion efficiency in both indoor and outdoor measurements from $(\eta_{in})_{bare}$=2.88% to $(\eta_{in})_{DC}$=3.82%, and from $(\eta_{out})_{bare}$=1.53% to $(\eta_{out})_{DC}$=2.15%, respectively. So, it provides an increase in both conversion efficiencies of $(\Delta\eta)_{in}$=32.69% and $(\Delta\eta)_{out}$=40.91%, respectively.

The optical properties of the dye-doped and undoped plates were measured and calculate. The peaks of absorbance spectrum of undoped plates (epoxy resin) and DC plates were at wavelengths of 340nm 380nm, respectively, the peak of fluorescence spectrum was at 422nm, and Stoke shift was $\Delta\lambda$=42nm at d=4mm.

The reflectance of 15% and refractive index of 2.3 were measured at wavelength of 422nm. The reflectance was decreased as the wavelength was increased.

References

[1] W.G.J.M. van Sark et al., "Improvement of spectral response of solar cells by deployment of spectral converters containing semiconductor nanocrystals", 19th Europ. Photovoltaic Solar Energy Conf. 2004, WIP Munich, ETA Florence, (2004) 38-41.

[2] C. Strümpel et al., "Enhancing silicon solar cell efficiency by modifying the solar spectrum", University of Konstanz, Faculty of Physics, Germany, (2006) 1-4.

[3] W.H. Weber and J. Lambe, *Appl. Opt.*, 15(10) (1976) 2299-2300.

[4] A. M. Hermann, *Solar Energy*, 29(4) (1982) 323-329.

[5] M.J. Currier, J.K. Mapel and M.A. Baldo, "Reduction of self- absorption in luminescent solar concentrators (LSC) using energy transfer in guest/ host films ", Molecular & Nanotechnology, MTL Annual research report (2007) 1-3.

[6] T. Trupke, P. Würfel and M.A. Green, *J. Appl. Phys.*, 92(3) (2002) 1668.

[7] H. Du et al., *Photochem. and Photobiol.*, 68 (1998) 141-142.

[8] M.S. Bhatnagar, "A Textbook of Polymer", Indian Institute of Technology, Kanpur, (3) (2004) 223-225.

[9] G. Boyle, "Solar Photovoltaic", *Renewable Energy U.S.*, (3) (1994) 90-136.

[10] A. Tupta, "Evaluating performance of photovoltaic cells" Keithley Instruments, Application Note B1500A-14 (2010) 1-15.

[11] T. Owen, "Fundamentals of modern UV-visble spectroscopy," Agilent Technologies, Germany, 5980 (2000) 1-148.

[12] M.S. Dresselhans, "Solid State Physics", Part Π: Optical Properties of Solid," (2002) 1-194.
[13] W. Williams, et al, *J. Phys. Chem.*, 98 (1994) 60-67.
[14] S.H. Al-Shaik Hussin, "Improvement efficiency of solar cell by using epoxy plates doped with rhodamine 6g dye", M.Sc. thesis, Department of Physics, University of Baghdad (Iraq) (2008) 71-99.
[15] D. Jameson, "Principles of Fluorescence Techniques", 5th Annual, Italy, 36 (2007) 1-92.
[16] J.A.M. van Roosmalen, *Semiconductors*, 38(8) (2004) 970-975.
[17] L.J. Wang, *Physics Essays*, 18(2) (2005).

This article was reviewed at School of Physical and Chemical Sciences, Faculty of Science, Queensland University of Technology, Brisbane, AUSTRALIA, Faculty of Built Environment and Engineering, School of Engineering Systems, Queensland University of Technology, Brisbane, AUSTRALIA, and School of Applied Sciences, University of Technology, Baghdad, IRAQ

Transmission of Compressed Video Signals through Spread Spectrum Channel

Awad Kh. Al-Asmari

Department of Electrical Engineering
King Saud University,
Riyadh, SAUDI ARABIA

This research studies the feasibility of devising a compression scheme for video sequences that is robust to fading errors in a spread spectrum environment. Schemes like subband coding and pyramid coding are inherently well suited for SS-CDMA environment and thus, pyramid coding is the chosen spatial decomposition scheme. Interframe coding using the two tap short symmetric filters reduces the complexity of motion adaptation techniques used in the MPEG standards. The various temporal low bands are vector quantized using the frequency sensitive competitive learning algorithm. For the temporal high bands, a simple method of geometric vector quantization is implemented. The coded bands are tested for robustness over a multi-path-fading channel at a vehicle speed of 65 mph. The simulation of channel is done according to the specifications of North American Digital Cellular Standard IS-95. The reconstruction of the coded bands results in image frames with average PSNR of 26 dB and average bit rate of 0.25 bpp. The subjective quality of these images is found to be satisfactory.

Keywords: Video sequences coding, Pyramid coding, Cellular image transmission

1. Introduction

The last decade has been a period of immense technological advancement, particularly in the areas of wireless and video communications. As the demand for multimedia communication services increases, mobility also becomes an important challenge for transmission of audio, data as well as visual information. As far as digital voice and data are concerned, there has been considerable progress in the past to identify major issues related to wireless and cellular radio environments. For instance, second-generation digital voice and data networks are developing rapidly and some are currently operational. However, despite its wide range of applications proven by a number of coding standards, video as a viable service for wireless multimedia communication has been relatively slow.

Currently a major challenge for video transmission is how to protect this sensitive signal against hostile radio environments. This is necessary because unlike the traditional error free media for which current coding standards have been designed, wireless channels do not offer guaranteed transmission. These channels can be corrupted by burst errors caused by environmental noise and, in the case of mobile communications, by multipath fading and shadowing.

The challenge of error-free transmission is further magnified because in order to comply with the low bit rate channel requirements, it is essential that video signal is compressed at very high compression ratio. Radio spectrum is a limited resource and is already congested due to existing wireless services. Compression methods can reduce the data rate in a digital video signal to a fraction of its original value by removing redundancy. But data compression makes the transmitted bit stream more vulnerable to channel errors. In an uncompressed digital video signal, an error in one bit might change the color or brightness of a pixel but there must be quite a few errors before they become noticeable to the eye. With compressed streams, however, a single bit error can cause much more noticeable image degradation since each bit encodes much more than a single point of the image.

Thus it is apparent that powerful techniques for digital compression are required while still maintaining an acceptable visual quality of the low bit rate video signals through noisy channels.

Recent works on digital image transmission over wireless channels have investigated image transmission in the IS-54 environment and achieved compression rates varying from 0.125 bpp to 0.35 bpp with image quality varying from a very good coarser approximation to a near original quality image [1,2]. In the DECT environment two studies have been investigated with a transmission rate in the range of 0.69 -to- 0.4 bpp [3,4]. But little work has been done so

 ISSN 1813-2065 Printed in IRAQ

far for image transmission by employing the well-known antimultipath spread spectrum technique. Since the CDMA technique is gaining popularity with the cellular industry giants such as QUALCOMM and Motorola, it presented an obvious choice for this research work. A very short summary and a primary result for the proposed algorithm can be found in [5].

The exploitation of spread spectrum scheme elegantly resolves the two basic technical challenges of terrestrial digital cellular networks: multiple user interference and multipath propagation [6]. The first issue is resolved because each user's signal appears as benign white noise to all other users, which can be eliminated by digital demodulation and error-correcting decoding processes. The fading resulting from multipath propagation is mitigated due to the frequency diversity inherent in wide-band systems. The multipath reflections are received as replicas of original signal, with different delays. The delayed signals can be separated, individually demodulated, and recombined constructively using RAKE receiver's [7], so that multipath can actually be exploited to improve performance of the CDMA system.

Another advantage of IS-95 standard resulting from the code division multiple access (CDMA) technique is the universal reuse of the entire allocated frequency band by every user of every cell. This improves efficiency as well as increases capacity per cell. Significantly, it also avoids the burdensome requirement for frequency planning, even when new cells are added in response to additional traffic needs.

The research aim in this paper is to achieve bit rates of 0.25 bpp for video transmission, to be tested in the spread-spectrum environment. It has been shown that multiresolution techniques like sub-band coding and pyramid coding are well suited for SS-CDMA [8]. The quantized pyramid levels of the decomposed image form multiple parallel data streams, each of which is multiplied by its unique spreading code. All the product signals are then transmitted at the same time in the same radio channel. Each received signal is independently recovered at the decoder by multiplying it with its spreading code and all the recovered subbands are then reassembled into a close reproduction of the original image. Thus, the proposed algorithm in this paper uses pyramid coding for spatial decomposition. Temporal decomposition is accomplished by the use of Short Symmetric-Kernel Filters [9], which offer the advantage of computational simplicity over the more complex methods, involved in any Motion-Compensation technique. The decomposed bands are coded using vector quantization (VQ). A neural network algorithm for vector quantization has been implemented. These algorithms are much faster than the classical ones as they process data in parallel. Another vector quantization scheme used is the geometric VQ [10], which is fast, simple and has a global codebook. The coded image sequence is tested in spread spectrum environment and analyzed for results. The wireless channel to be simulated for image transmission is chosen to be the CDMA-based North American digital cellular standard IS-95A.

The paper is organized as follows. We begin with a general overview of the 3-D decomposition of the image sequence in section two. Then, we describe the vector quantization design by using the neural network and its implementation for image coding in section 3. The vector quantization design for the low frequency bands and the high frequency bands are discussed in section four. The performance of the proposed algorithm is compared with the performance of MPEG standard algorithm in section five. The CDMA wireless channel is presented in section six. This simulation is conducted on Cadence's signal processing software SPW. In section seven, the overall compression algorithm is tested on video sequences with different activates. The simulation is done at 0.25 bpp at two vehicle speeds (0 mph and 65 mph). The conclusion of this work is presented in section eight.

2. 3D Decomposition of Image Sequence

Extending spatial filtering to three dimensions can make use of the temporal redundancy existing between the subsequent frames of a video sequence. Temporal filtering is achieved by applying the two-tap Haar filter, resulting in a temporal high band which contains sparse information, consisting of most of the high frequency motion components, and a highly correlated temporal low band.

The temporal low band is further filtered by applying the spatial 24-tap FIR filter given in [11]. Since this filter allows a decimation factor of four, greater compression ratio is possible here. But due to the sparse nature of information in the temporal high band, this filter does not work very well with it. The 5-tap Gaussian filter is used to decompose the temporal high band. The whole decomposition process is shown in Fig. (1). In this decomposition process, most of the signal energy resides in the lower spatial frequency bands, namely bands 1 and 2. Subband 4, which corresponds to the high temporal/low spatial frequencies, carries most of the motion information and acts as a motion detector. Thus, by accurate coding of low spatio-temporal bands, the spatial details of the original image are conserved, and by careful encoding of band 3,

most of the motion information will be preserved.

Once the original image has been decomposed and the redundancy in the data removed, next step in the image compression problem is to code the constituent bands. Vector quantization schemes have been found to be more effective here as compared to scalar quantization according to Shannon's rate distortion theory. In the next sections we discuss the two steps required during the quantization process: design of the codebook and matching the input vectors to the best possible code vector from the codebook.

Different techniques involving vector or scalar quantization can be used to encode the decomposed pyramid levels. From Shannon's rate distortion theory, it can be shown that vector quantization can achieve better compression performance than any other conventional coding technique which is based on encoding of scalar quantities. However, practical application of VQ techniques has been limited because of the prohibitive amount of computational complexity and time involved with the classical encoding algorithms such as the Linde-Buzo-Gray (LBG) algorithm [12].

Recently a number of studies have proposed the use of artificial neural network (ANNs) as a powerful technique for implementing VQ [13]-[15]. Neural network approaches appear to be more promising for intelligent information processing as a result of their massively parallel computing structures and self-organizing learning schemes. These algorithms are much faster than the classical ones as they process data in parallel. They have been found to be less sensitive to initial conditions, have fast convergence properties, and have the ability to produce a lower mean distortion codebook. Moreover, when the ANNs are implemented in hardware, vector quantization can be done in real time since the networks have highly parallel structure [16].

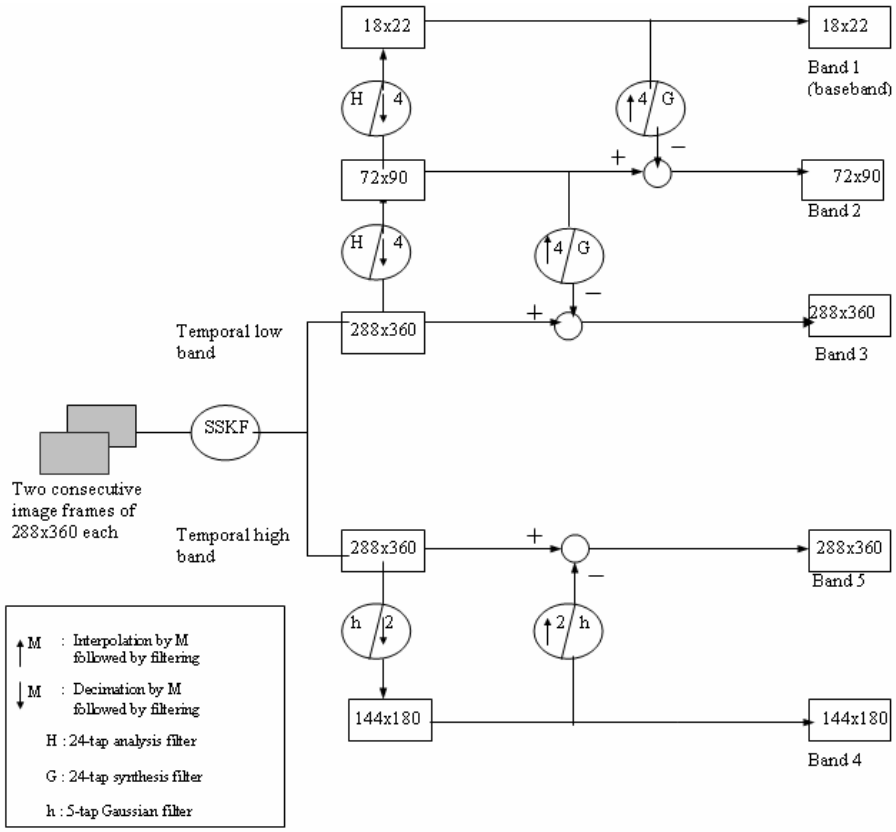

Fig. (1) Three dimensional decomposition of video sequence

The architecture of ANNs basically consists of an input layer and an output layer. The layers are dense interconnections of simple processors, or neurons, which operate in parallel. Each interconnection is associated with a weight factor w_k. These weights are usually trained on one or more images so that they develop an internal representation corresponding, not to the image, but rather to the relevant features of a class of images.

One of the important purposes of neural VQ is to create an ordered mapping from a high-dimensional input space to a low-dimensional output space, and to extract meaningful features from the input data. Kohonen's self-organizing maps (SOFMs) have been regarded as one of the

 ISSN 1813-2065

most powerful network in that sense. The work of Nasrabadi and Feng [13] has shown SOFM to give better results than the traditional LBG algorithm in the sense of the mean expected distortion. Kohonen's SOFM also addresses the problem of underutilized neural units faced by many other neural network algorithms. In many of the learning methods, the frequency of use of entries in the codebook can be quite uneven, leaving some codewords as underutilized. Kohonen's SOFM ensures that all codewords are doing their fair share in representing the input data by associating with each neural unit, a neighborhood of other neural units. During the training process, the winning neural unit as well as the neural units in the neighborhood of the winner are updated. Thus, by the use of neighborhoods, the SOFM network overcomes the problem of underutilized nodes, but at the expense of additional computation involved during training. This additional computation arises from both the calculation of the neighborhood of the winning unit, as well as from the updating of all members of the neighborhood.

This research uses the frequency-sensitive competitive learning (FSCL) network [14]. One of the motivations for this is that it overcomes the limitations of underutilized networks while retaining the computational advantages of its neural structure. In the FSCL network, each neural unit incorporates a count of the number of times it has been the winner. This information is used to ensure that, during the course of the training process, all neural units are modified an approximately equal number of times. This is done by modifying the distortion measure used to determine the winner. The distortion measure is weighted by an increasing function of the number of wins for each unit. In this way, units that have had many wins, i.e. which are over utilized, are less likely to be chosen for modification, giving other units with a lower count value a chance to win the competition.

Specifically, let $d(x,w_i(n))$ be the distortion measure that is to be minimized during the quantization process, and let $u_i(n)$ be the total number of times that a neural unit i has been the winner during training. Then a modified distortion measure for the training process is defined as:

$$d^*(x,w_i)=d(x,w_i(n))*u_i(n) \quad (1)$$

The winning unit at each step of the training process is the one with the minimum d^*. If a given neural unit wins the competition frequently, its count and consequently d^* increases. This reduces the likelihood that this unit will be the winner.

The FSCL network architecture consists of three layers:

- an input layer that distributes the input vector from the training set to the second layer
- a second layer of units, where each unit computes the modified distortion d^* between its weight vector (code vector) and the input vector
- an output layer based on the minimum distance criteria that determines the winning neural unit from the distortions computed by the second layer units.

Thus there are N neural units in the input layer, and M units in the middle and output layers, where N is the dimension of the input vector, and M is the size of the codebook, i.e. the number of codevectors in the codebook.

The code vectors of the winning neuron are updated according to the one iteration learning rule described below:

- The codevectors W_i and the winning frequency associated with each codevector, F_i are all initialized for each distortion computing neuron in the second layer.

$W_i(0)$=R(i) and $F_i(0)$=1, i = 1, 2, ..., M

Here R(i) are the initial codevectors, taken from a random vector-number generating function.

- The distortion D_i(t) between an input vector X(t) and all the code vectors W_i(t) is calculated as:

$$D_i(t)=\sum_{j=1}^{N}\left(X_j(t)-W_{ij}(t)\right)^2 \quad (2)$$

where t is the training iteration index

- The distortion computing neuron with the smallest distortion is designated as the winning neuron and its output is: W_i(t+1)=W_i(t)+C(t)*out$_i$(t)*[X(t)-W_i(t)] where C(t)=$\frac{1}{F_i(t)}$, if $1 \le F_i(t) \le F_{thr}$ and 0, otherwise.

Here, C(t) is the frequency sensitive learning rate and F_{thr} is the upper threshold frequency. In this research, an upper threshold of 250 is found to be adequate to allow training of the codebook.

- The above steps are repeated for all the training vectors X(t). The final codebook obtained is an optimal codebook.

3. Designing the Code Books for Vector Quantization

The neural network algorithm FSCL (Frequency Selective Competitive Learning) discussed in the previous section is used for the design of the codebook for vector quantization. Our research involves design of two separate codebooks, one for the high frequency edge vector patterns, and one for the approximately stationary vector patterns. The reason for designing two separate code books is that while most of the vectors in the baseband (band 1) have low variance and are almost stationary, the vectors found in band 2 and 3 are mostly edge

patterns and show high variances. So to have a good representation for both kinds of input vectors, separate training sets have been used to simulate each codebook. Several different images are used for the purpose of the training set: the images are filtered into their low pass and high pass components and then used to simulate the neural network clustering technique. Once the codebooks are formed, the actual quantization occurs as follows.

Since most of the energy of the decomposed image is concentrated in the lowest spatio-temporal frequency band, also called the baseband (band 1), the dimension of the stationary codebook is kept quite small and is chosen as 4. Also, since the baseband contains only the slowly varying information content, its 4-dimension vectors do not exhibit widely varying geometric patterns. Thus, a small-sized codebook is sufficient to represent all the vectors in this band. A codebook of size 64 was chosen for this work.

The second level in the pyramid has the high-frequency content of the decomposed temporal low band and requires a separate codebook for its coding. This codebook has been trained on data that has highly varying edge content so that it can faithfully code data of similar nature. The size of this codebook is 256 and dimension 4.

The first difference level (band 3) in the pyramid has the minimum information most of which is concentrated around the edges. This information can be coded by applying an edge detector to find the location of pixels that are perceptually important and then transmitting only these coded pixels. But this would also require the transmission of the position of these coded locations to the receiver in order to reconstruct this band. To avoid this, a scheme of predicting the edges of band 3 from band 1 and 2 is used. This is shown in Fig. (2).

Before coding, the baseband is interpolated to the second level and added to band 2. This is further interpolated to the size of the original image. Edge-detection is applied to this up-sampled version and the corresponding pixels from the first difference level are formed into vectors and quantized. At the receiver, similar process is repeated by upsampling the quantized baseband, adding it to the quantized second level, and then upsampling it to the original image size. This partially reconstructed version of the original image is used for edge-detection which gives the location of the vectors of the band 3 that are coded. Once the locations are known, the coded vectors are suitably placed to form band 3. Thus, using this approach, no side information needs to be sent for the coded areas of the first difference image level and an average of only 4% to 5% of this level needs to be coded. Thus, more compression is achieved by edge-detection instead of coding the band as it is.

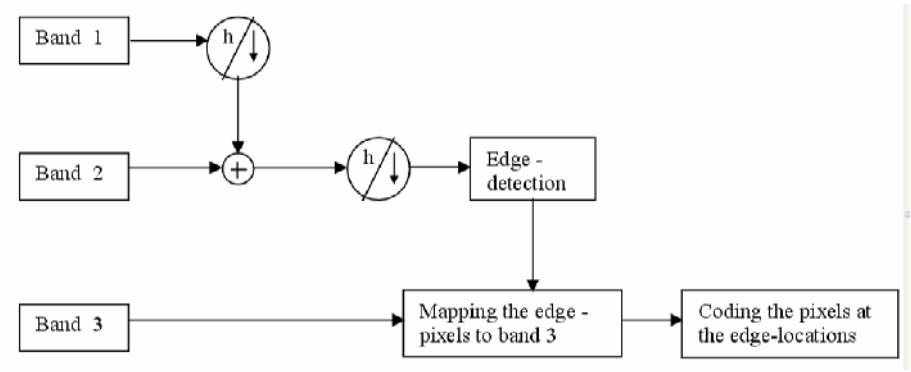

Fig. (2) Coding of edge location in band 3 using band 1 and 2

Bands 4 and 5 form the pyramid levels of the decomposed temporal high band. The subbands whose energy falls below an empirically derived threshold value are discarded without causing severe degradation to the reconstructed image. Band 5 has extremely low energy content and the sparse information carried in it is not significant in the final image reconstruction, thus it can be safely discarded. The coding process for band 4 is discussed below.

This is the nondominant subband that contains a small amount of the total signal energy yet data that is perceptually very significant as it contains most of the sharp edge and contour information as well as the fast motion aspects. The neural vector quantization approach used for the decomposed temporal low band does not work very well for this. Instead, a perceptually efficient image coding scheme is required that can preserve the underlying edge geometries in the high frequency signals at low coding rates. A geometric vector quantization (GVQ) scheme proposed in [10] is adapted in this paper where the code vectors are derived from a small set of local geometric patterns found in the high-frequency subbands. This method takes advantage of the human eye's sensitivity to sustained intensity changes as found in an edge.

ISSN 1813-2065

In general, the GVQ method provides an optimum *l*-level scalar quantizer for each data vector for a given error metric. In this paper, a two level GVQ based on the minimum mean square error (MMSE) criterion is used. Unlike traditional VQ, GVQ does not require a training set for its codebook design. Instead, it makes use of the fact that the high-frequency bands have a lot of edges that can be represented by typical geometric shapes. Thus a codebook of simple geometric shapes like strips or strip combinations of various orientations and thickness is sufficient to represent this data. The code vectors for two-level GVQ are binary valued blocks reflecting these basic shapes. Each coded block is accompanied by two locally adapted intensity values, representing the binary values of the block. The dimension of the code vectors is chosen to be 3x3 blocks, so an exhaustive binary codebook of all possible shapes can be formed by 2^{9-1}=256 code vectors. The other 256 code vectors are just the complements of the first 256 code vectors. The latter codebook gives better results as compared to a codebook of elementary shapes.

The image is divided into 3x3 non-overlapping subblocks of input vectors. For a given input vector, an adaptive procedure modulates the two intensities of each code vector, and the code vector with the best match is used to reproduce the input image block. The transmitted information includes the index k_{best} of the chosen code vector as well as its chosen intensity levels L_1 and L_2. The index k_{best} is given by 8 bits and each of the intensity values L_1 and L_2 is represented by a uniform 5-bit scalar quantizer.

4. Performance Evaluation of the Compression Algorithm

The performance of the proposed algorithm is compared with the performance of MPEG standard algorithm. The MPEG standard does not give detailed rules of how a sequence should be coded. The standard is like a protocol for the decoding procedure. The broad guidelines for achieving good compression are mentioned but many choices are left for the user to decide. Thus the comparison made here with MPEG is more analytical than experimental.

The visual quality of the reconstructed sequence is excellent in both algorithms. The reconstructed sequence is almost indiscernible from the original sequence.

The performance of the two algorithms is compared based on the signal to noise ratio, and the bit rate (bpp) requirements. The average PSNR of the reconstructed Miss America sequence using MPEG is approximately similar to the PSNR that can be achieved with the algorithm presented in this paper. The algorithm introduced presents a major advantage over MPEG here, by supporting the possibility of progressive transmission of the video signal. The bits per pixel (bpp) requirements for both algorithms are very similar.

The transmission and reception of the compressed bands through a CDMA wireless channel is depicted below in Fig. (3). The actual simulation has been done using Cadence's signal processing software SPW. The simulation files used have been shown in Appendix A. Although CDMA technology allows transmission of all the coded bands at the same time unlike the TDMA technique, to avoid complexity of diagram, the transmission of only one band is shown in the Fig. (3). But in the actual simulation of the channel, two coded bands have been transmitted simultaneously. Walsh codes 1 to 4 have been used to separate data of one band from the other band.

Once the image has been compressed by the image coder, it is error-protected by using a convolutional code (2, 1, 5), n=2; k=1; m=5. Further, to combat the burst errors associated with a fading channel, the error-protected data is interleaved. Interleaving spreads out the data in time so that burst errors are spread out to appear independently making a bursty channel similar to an AWGN channel. The interleaved data is modulated using a QPSK modulator and the in-phase and quadrature components of the output are spread by PN sequences. The I-channel PN generator function is '0121641' and the Q-channel PN generator function is '0116171'. The spreading factor is 128 as specified by the IS-95A standard with a bit rate of 9600 bps and chip rate of 1.2288 Mcps. Walsh functions from 1 to 4 are used for the four bands. A square root raised cosine filter with a roll-off factor of 0.35 is used for pulse shaping and the data is fed through a frequency selective multipath fading channel. White noise corresponding to 18 dB channel SNR is added to the output of the fading channel. At the receiver end, the data is again filtered by the same filter used for pulse shaping. Despreading takes place and the despread data is demodulated. The deinterleaver is used to record the data back to its original sequence. After passing through a convolutional decoder, the data is sent to the image decoder for reconstruction of an approximation of the original frames.

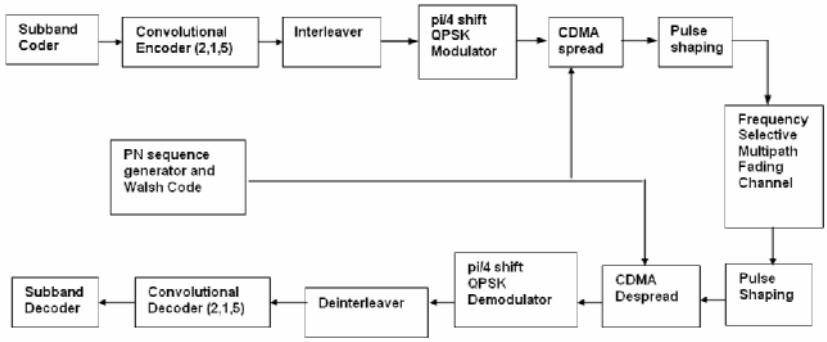

Fig. (3) IS-95A Standard specification for transmission and reception across a wireless channel

5. Simulation Results

The compression algorithm is tested on two sequences, one with slow motion and static background, and the other with faster motion and noisier background. Both are gray-scale sequences having 288×360 pixels per frame at the rate of 30 frames /s.

This research is aimed at compressing video sequences at 0.25 bpp at vehicle speed of 65 mph. The bit rate calculations of 0.25 bpp or less for the Miss America sequence is shown in Table (1) for two frames. Simulation results have been obtained for two frames each from both these sequences. Quantitative evaluation involving the calculation of the peak-signal-to-noise ratio (PSNR) as well as qualitative analysis is performed to judge the quality of the image sequences.

Table (1) Bit rates and PSNR for slow motion and static background sequence

Band	Bit rate	PSNR	Average Bit rate
Band 4	1.01	33.97	1.01/4 = 0.25 bpp
Band 3	0.08	32.31	0.08 bpp
Band 2	2.0	34.56	2/16 = 0.125 bpp
Band 1	1.5	38.64	1.5/256 = 0.03 bpp
			0.245 bpp

For a more subjective evaluation of the results presented above, the mean opinion score (MOS) is used as a basis to reflect the quality of the image. A number of viewer rate the image according to how appealing it is visually, and the mean of these ratings gives the MOS. The results presented before were compared side by side with the original images by ten viewers. The MOS scales for the two test frames of Miss America sequence and the Salesman sequence are given in Table (2).

Table (2a) MOS Results for the slow motion and static background sequence

Channel SNR and Vehicle Speed	MOS
0 dB SNR, 0 mph	4.75
18 dB SNR, 0.1 mph	4.50
18 dB SNR, 65 mph	3.25

Table (2b) MOS Results for faster motion and noisier background sequence

Channel SNR and Vehicle Speed	MOS
0 dB SNR, 0 mph	4.60
18 dB SNR, 0.1 mph	4.25
18 dB SNR, 65 mph	3.50

5. Conclusion

In this paper, a novel compression scheme for video sequences that is robust for fading error in a spread spectrum environment is presented. A 3-D coder has been designed in which the sequence is decomposed into spatio-temporal sub-bands. The proposed algorithm involves the design of two separate code books, one for the high frequency edge vector patterns and one for the approximately stationary vector patterns. The encoded bands are sent through a channel based on IS-95A (North American digital cellular standard) specifications and the bands are later combined to recover the original sequence at the image decoder.

The slow motion and static background compressed sequence can be transmitted at a rate of 715 Kbps and the faster motion and noisier background sequence requires 793 Kbps. Vehicle speeds of 0.01 mph and 65 mph are considered which represent two extreme channel conditions: stationary and rapidly time-varying, at channel SNR 18 dB. The PSNR of the frames in the presence of fading errors was found to vary between 25 dB to 28 dB. Most of the degradation in performance is attributed to errors in the baseband. Errors in the lower levels do not significantly affect the image quality. Performance can be improved by increasing the channel SNR to be more than 18 dB (22 dB for example). Moreover, the baseband can be transmitted without any compression. This would augment the bit rate by 0.03 bpp but will make the transmitted images more robust to channel errors.

References

[1] A. Al-Asmari, V. Singh and S. Kwatra, S. "Hybrid Coding of Images for Progressive

 ISSN 1813-2065

Transmission over a Digital Cellular Channel", Proc. IEEE/CISST'99, Monte Carlo Resort (Nevada, 1999).
[2] Y. Zhang, Y. Liu and R.L. Pickholtz, *IEEE Trans. on Vehicular Technol.*, 43(3) (1994) 786-794.
[3] N.M. Nasrabadi and E.S. Jay, *IEEE Trans. on Circuits and Sys. for Video Technol.*, 5(3) (1995) 247-253.
[4] A.Kh. Al-Asmari, "Multiresolution Image Coding for Wireless Channel", Proc. IEEE/ICCE'98 (CA, 1998) 38-39.
[5] A. Al-Asmari, D. Arya and S. Kwatra, *Electron. Lett.*, 36(5) (2000) 465-566.
[6] A.J. Viterbi, *IEEE Trans. on Vehicular Technol.*, 43(3) (1994) 638-643.
[7] R. Price and P. Green Jr., *Proc. IRE*, 46 (1958) 555-570.
[8] B.C. Wang and P.R. Chang, *IEEE Trans. on Circuits and Sys. for Video Technol.*, 6(2) (1996) 200-214.
[9] G. Karlsson and M. Vetterli, *Opt. Eng.*, 27(7) (1988) 574-586.
[10] C. Podilchik, N. Jayant and N. Farvardin, *IEEE Trans. on Image Process.*, 4(2) (1995) 125-138.
[11] A.Kh. Al-Asmari, *IEEE Trans. on Circuits and Sys. for Video Technol.*, 5(3) (1995) 182-192.
[12] Y. Linde, A. Buzo and R.M. Gray, *IEEE Trans. on Commun.*, COM-28 (1980) 84-95.
[13] N.M. Nasrabadi and Y. Feng, "Vector Quantization of Images based on Kohonen Self-Organizing Feature Maps", Proc. of the IEEE Int. Conf. on Neural Networks, San Diego, 1 (1988) 101-108.
[14] S.C. Ahalt, *IEEE J. on Sel. Areas in Commun.*, 8(8) (1990).
[15] C. Cramer, E. Gelenbe and H. Bakircioglu, *Proc. of IEEE*, 84(10) (1996) 1529.
[16] R.P. Lippman, *IEEE ASSP Magazine*, (1987) 4-22.

This article was reviewed at School of Engineering Systems, Queensland University of Technology, Brisbane, AUSTRALIA, and School of Applied Sciences, University of Technology, Baghdad, IRAQ

Emad S. Ahmed

A CPW-Fed Printed Monopole Ultra-Wideband Antenna with E-Shaped Notched Band Slot

Department of Electrical and Electronic Engineering University of Technology, Baghdad, Iraq

A coplanar waveguide (CPW) fed printed monopole ultra-wideband antenna with E-shaped notched band slot is presented. This antenna is fed by a 50Ω CPW line and it is fabricated on the FR-4 substrate with a thickness of 1.5 mm and relative dielectric constant of 4.4. Two modifications are introduced on this antenna to improve its operating bandwidth. The first one is to remove a 90° angles from the two upper corners of the ground plane by blending them in a radius of 10mm. The second modification is to chamfer the feed edges at the patch. All simulations in this work were carried out by using CST Microwave Studio™ package. Compared with the recently proposed antennas, the proposed antenna has wide bandwidth with acceptable returned losses, compact in size and easy design, easy controllable band-notch characteristics and good gain characteristics over the entire desired bandwidth.

Keywords: Ultra wideband, Coplanar waveguide, Band-notch, UWB antenna
Received: 29 October 2010, **Revised**: 03 December 2010, **Accepted**: 10 December 2010

1. Introduction

Ultra wideband (UWB) technology has become one of most promising technologies in wireless communications since the federal communications commission (FCC) has released the 3.1-10.6 GHz frequency band in 2002 for UWB technology and applications [1]. Many different types of antenna are being considered for UWB applications. Among these antenna configurations, circular monopole features simple structure, easy fabrication, wide frequency bandwidth and satisfactory radiation patterns [2,3].

However the designated band overlaps with the HIPERLAN/2 bands (5.15-5.35 GHz, 5.470-5.725GHz) and the IEEE 802.11.a bands (5.15-5.35GHz, 5.725-5.825) which can interfere with the UWB communication systems. Therefore, the UWB antenna with a band notched characteristics is required to reduce the interference. Researchers in some literatures produce band rejection characteristics by cutting a slot on the antenna, or adding a tuning metal stub within the antenna structure [4,5]. The antenna notched band is simile to the virtual-open or virtual-short circuit and is capable of not only preventing energy from transmitting to free space, but of also avoiding receiving the unwanted signal from free space [6,7].

In this paper a new design for printed CPW fed elliptical monopole antenna with notched slot were presented. The notched frequency band is adjustable by varying the length and location of the slot. This antenna can cover UWB frequency range (3.1-20 GHz) and rejects the limited (5.15-5.825 GHz) band. To understand the behavior of the antenna model and to obtain the optimum parameters, the simulation was performed with CST Microwave Studio™ package based on transient time solver method.

2. Antenna Design

The proposed geometry of the antenna is presented in Fig. (1) and the parameters are summarized in Table (1). This antenna is consist of elliptical patch fed by a 50Ω CPW line with rectangular ground plane and has a dimension of 22.2×26.5 mm^2 that is fabricated on the FR-4 substrate with a thickness of 1.5 mm and relative dielectric constant of 4.4. The proposed antenna is located in x-y plane and the normal direction is parallel to z-axis.

Table (1) Antenna parameters, mm

ℓ_1	26.5	S_1	9.6
ℓ_2	22.2	S_2	2.4
ℓ_3	9	S_3	2.2
ℓ_4	9	S_4	0.7
ℓ_5	5.6	S_5	0.8
ℓ_6	4.1	S_6	5.5
$2A$	17.5	S_7	1
$2B$	13	t	0.07
g	0.3	w	3.6
h	1.5	ε_r	4.4

It has been shown in literature that the -10 dB operating bandwidth of UWB antenna can be enhanced significantly by using tapered microstrip or CPW feeding line, arc shaped patch and tapered ground plane [8-11]. Accordingly, two modifications are introduced on the

proposed antenna to improve its operating bandwidth. The first one is to remove a 90° angles from the two upper corners of the ground plane by blending them in a radius of 10mm. The second modification is to chamfer the feed edges at the patch with 15° angle and distance equal to 4.1mm.

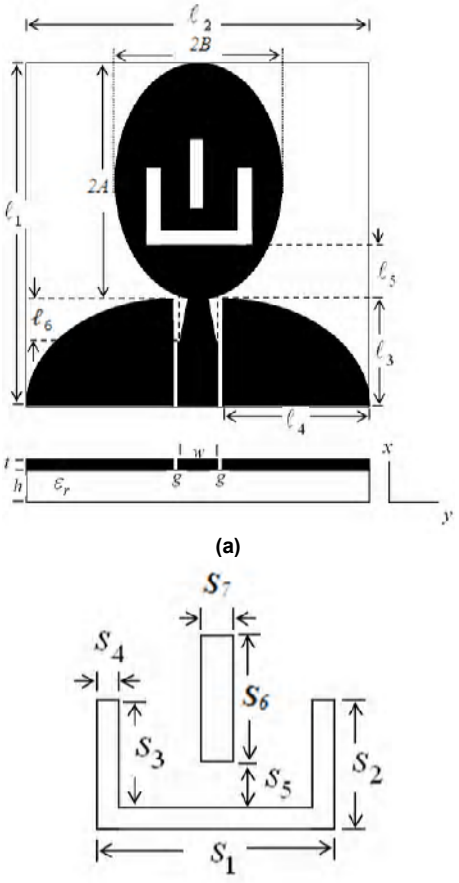

(a)

(b)

Fig. (1) Configuration of proposed antenna: (a) Top view (b) Proposed cutting slot

As depicted in Fig. (1), a thin E-shaped slot is etched in the interior of the radiating element. The presence of the slot produces an additional resonance mode in the structure, called slot mode, which is responsible for the degradation of the input impedance of the antenna at certain frequencies, i.e., within the notched frequency band [12]. Resonance of the slot occurs, when the length of its external perimeter is approximately half wavelength of the notched band center frequency and given by:

$$\frac{\lambda}{2}_{Notched} = 2(S_1 + S_2 + S_3) \qquad (1)$$

The notched center frequency can be adjusted by tuning the length of the U shape slot and the notched depth can be slightly adjusted by optimizing the length S_6 of the middle slot.

3. Antenna Simulation Results

In this section analysis of the proposed antenna are obtained by using CST Microwave Studio ^{TM} package. Figure (2) shows the simulated return loss S_{11} for the proposed antenna. As shown in Fig. (2), the effect of modifications is clearly illustrated. It can be noticed that chamfering the edge of the feeder near the patch has more effect than blending the upper edges of the ground plane. Both modifications have a considerable effect on the performance of the return loss of the antenna. The proposed antenna satisfies the -10dB return loss (VSWR<2) requirements from 3GHz-20GHz. The proposed antenna can cover the frequency band 3.1 to 10.6 released by FCC for UWB system for VSWR<2 and rejected band from 5-6 GHz.

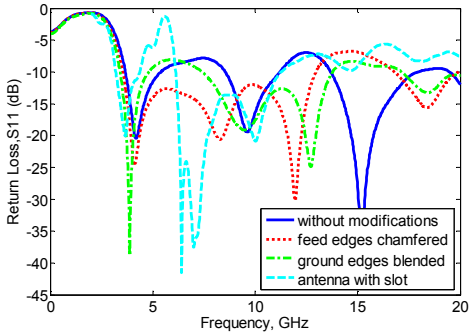

Fig. (2) Return loss of the proposed antenna

Figure (3) shows the simulated VSWR performance of the proposed antenna. The simulated bandwidth of the antenna ranges from 3.1 to more than 11GHz for VSWR less than 2. It is also observed that the sharp frequency band-stop characteristic is obtained much closed to the desired frequency of 5.5GHz when an E-shaped slot with the optimized dimensions given in Table (1) is inserted into the antenna structure.

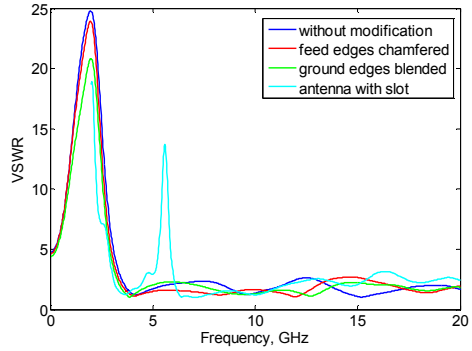

Fig. (3) Simulated VSWR for the proposed antenna with E-slot

Figure (4) shows the current distributions at 4, 5.5, 6.5, and 10.5 GHz. At notched band center frequency 5.5 GHz, it reveals that, current distribution concentrate over the area of the slot

more and stronger than any other area. It seems that, exciting the slot mode in the radiating structure, play a role in a band notched filter [9,12,13].

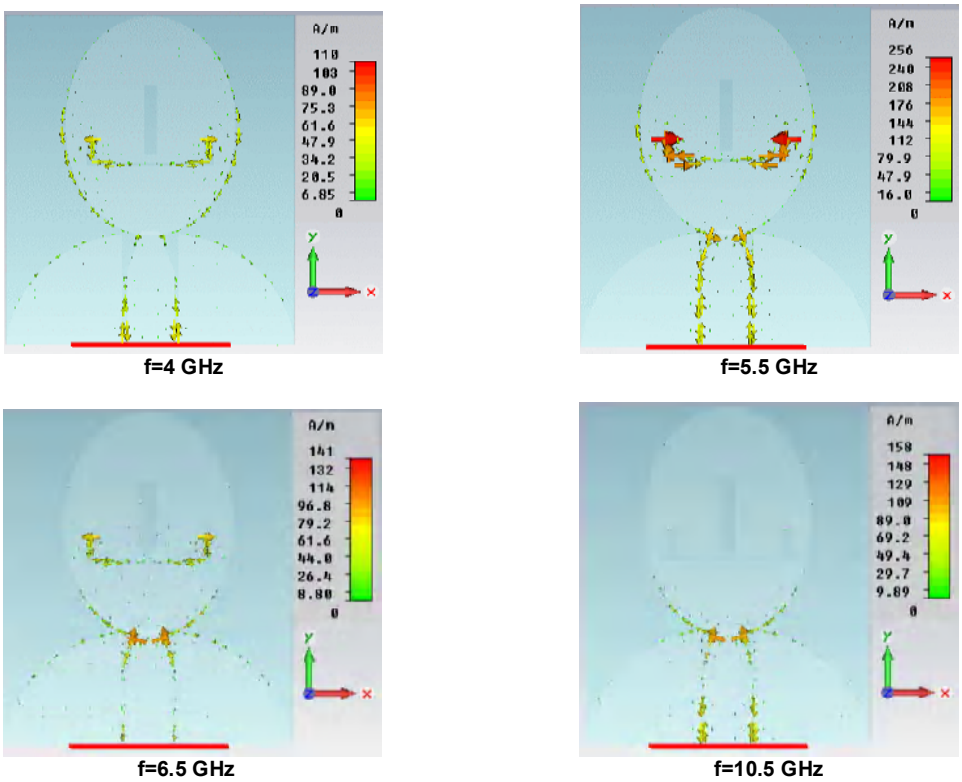

Fig. (4) Current distribution at 4 GHz, 5.5 GHz, 6.5 GHz and 10.5 GHz

Figure (5) shows the simulated radiation patterns for the proposed antenna at 3.5GHz, 6.5GHz, 8.5GHz and 10.5GHz frequencies. The proposed antenna has an acceptable Omni-directional pattern required to receive signal from all directions.

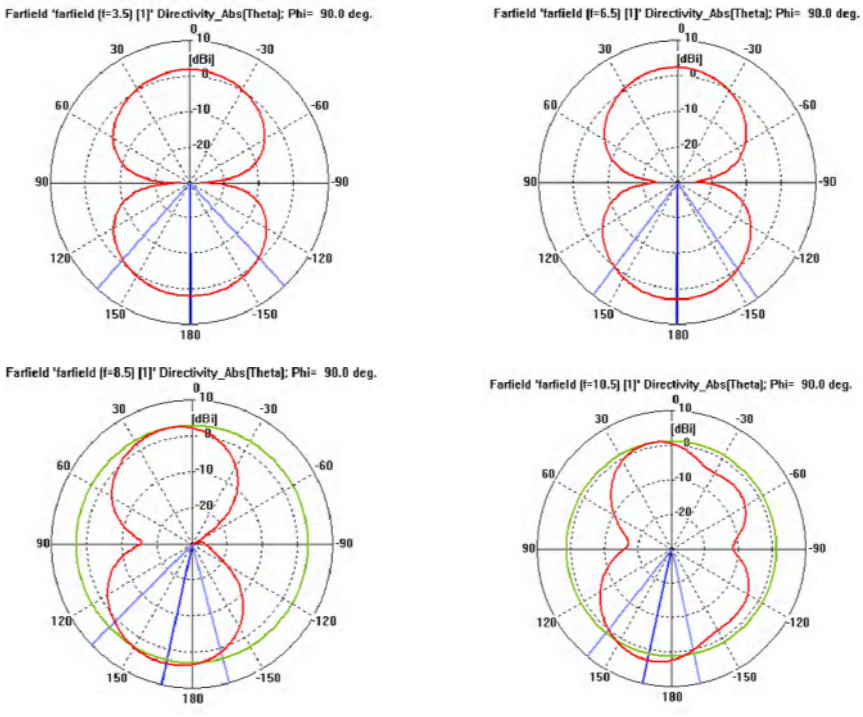

Fig. (5) Polar plot of far-field antenna pattern at selected frequencies

ISSN 1813-2065

The antenna gain is varying from about 2.84dBi to 5.68dBi across the entire bandwidth. Figure (6) shows the 3D plot of the field pattern of the proposed antenna at selected frequencies and the gain value at each of the selected frequencies.

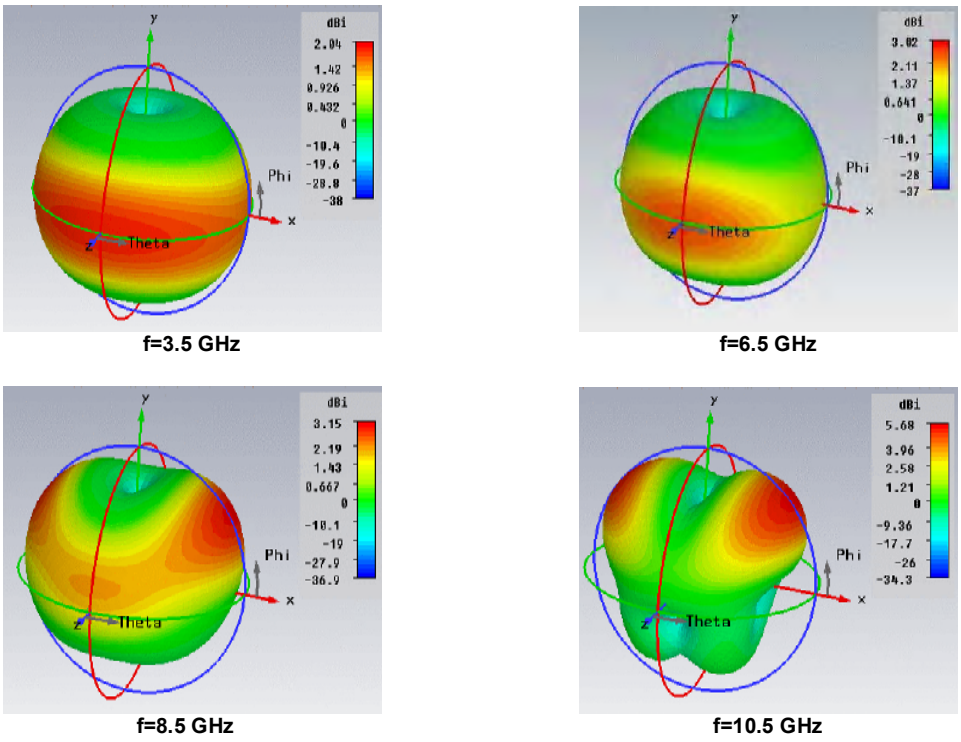

Fig. (6) 3D plot of field pattern shows the gain at each selected frequency

Table (2) presents a comparison between the performance of some recently UWB antennas that cover the UWB band from 3.1-10.6 GHz and the proposed antenna. The proposed antenna shows wide impedance bandwidth, compact size, narrow selective notched band and good gain features.

Table (2) Comparison between recently proposed antennas and this antenna

Antenna	Simulated Bandwidth (GHz)	Simulated Notch Bandwidth (GHz)	Notch Slot Type	Antenna Size (mm^2)	Gain (dBi)
This work	3-20	5-6	E-Shaped	22.2x26.5	2.84-5.68
[7]	2-12	5.24-6.46	Resonator	35x30	Not defined
[13]	3-23	5-6	C-Shaped	28x30	0.2-3.9
[14]	2-12	4-6.5	E-Shaped	35x35	Not defined

4. Conclusion

In this paper, a novel CPW-fed printed UWB antenna with band rejection E-shaped slot is proposed. The proposed antenna design begins from simple printed elliptical monopole fed by 50 Ω CPW with rectangular ground plane. Two modifications are proposed to enhance the -10 dB UWB characteristics. It can be noticed that chamfering the edge of the feeder near the patch has more effect on impedance matching than blending the upper edges of the ground plane. Both modifications have a considerable effect on the performance of the return loss of the antenna. The notched frequency band covers the WLAN frequency range for interference reduction between UWB and WLAN system. By adjusting the dimension of the slot, it can obtain the desired band-notched characteristics. The proposed antenna has wide bandwidth with acceptable returned losses, compact in size and easy design, easy controllable band-notch characteristics and good gain characteristics over the entire desired bandwidth.

References

[1] Federal Communication Commission, "First Report and Order, Revision of Part 15 of the Commission's Rules Regarding Ultra-Wideband Transmission System", FCC 02 48, 2002.

[2] P.A. Narayan, K. Girish and K.P. Ray, *IEEE Trans. on Antennas and Propag.*, 46(2) (1998) 294-295.

[3] Y.-L. Kuo and K.-L. Wong, *IEEE Trans. on Antennas and Propag.*, 51(9) (2003) 2187-2191.

[4] J. Qiu et al., *IEEE Trans. on Antennas and Propag.*, 54(1) (2006) 288-292.

[5] T. Dissanayake and K.P. Esselle, *IEEE Trans. on Antennas and Propag.*, 55(11) (2007) 3320-3325.
[6] K.H. Kim and S.O. Park, *IEEE Trans. on Antennas and Propag.*, 54(6) (2006) 1688-1692.
[7] W. Sung-Jung et al., *IEEE Trans. on Antennas and Propag.*, 58(6) (2010) 1890-1897.
[8] P. Kabacik, P. Opalka, and P. Hornik, "TTC Patch Antennas Made in a Conformal Form with Small Radius", Proc. EuCAP 2006, Nice, France, 6-10 November 2006.
[9] F. Yu and C. Wang, *Radioeng.*, 18(4) (2009) 551-555.
[10] K. Yin and J. Xu, "Compact Ultra-wideband Monopole Antenna with Band-stop Characteristic", In International Conference on Microwave and Millimeter wave Technology, vol. 3, Nanjing (China), pp. 1174-1176, 2008.
[11] R. Chair, A. Kishk and K. Lee, *IEEE Antenna and Wireless Propag. Lett.*, 3(12) (2004) 227-229.
[12] A.D. Eva et al., *IEEE Trans. on Antennas and Propag.*, 58(5) (2010) 1457-1467.
[13] S.J. Kim, J.W. Baik and Y.S. Kim, "Design of A UWB Slot Antenna with frequency Band-notched Characteristic", Inter. Symp. on Antenna and Propagation, ISAP 2006.
[14] Q. Chengwei et al., "Hybrid Shaped Band-Notched Ultra-Wideband Patch Antenna", Proc. of Inter. Symp. on Antennas and Propagation, ISAP 2007, Niigata, Japan.

This article was reviewed at Department of Electronic and Electrical Engineering, Loughborough University, Leicestershire, UK, and School of Applied Sciences, University of Technology, Baghdad, IRAQ

Einstein-Szilard Refrigerator

Albert Einstein is best known to the general public for devising the world's most famous equation: E=mc2. But his contributions to physics extend over a broad range of topics, including Brownian motion, the photoelectric effect, special and general relativity, and stimulated emission, which led to the development of the laser. Less well known, even among physicists, is his work with Leo Szilard to develop an energy efficient absorption refrigerator with no moving parts.

Szilard was born in Budapest, Hungary in 1898, the son of a civil engineer, and served in the Austro-Hungarian Army during World War I. After the war, he returned to university, studying physics under Einstein and Max Planck, among others. His dissertation was in thermodynamics, and in 1929 he published a seminal paper, "On the Lessening of Entropy in a Thermodynamic System by Interference of an Intelligent Being"–part of an ongoing attempt by physicists to better understand the "Maxwell's Demon" thought experiment first proposed by James Clerk Maxwell in the 19th century.

Szilard had a knack for invention, applying for patents for an x-ray sensitive cell and improvements to mercury vapor lamps while still a young scientist. He also filed patents for an electron microscope, as well as the linear accelerator and the cyclotron, all of which have helped revolutionize physics research. Szilard's most important contribution to 20th century physics was the neutron chain reaction, first conceived in 1933. In 1955, he and Enrico Fermi received a joint patent on the first nuclear reactor.

Einstein wasn't a stranger to the patent process, either, having worked as a patent clerk in Bern as a young man. He later received a patent with a German engineer named Rudolf Goldschmidt in 1934 for a working prototype of a hearing aid. A singer of Einstein's acquaintance who suffered hearing loss provided the inspiration for the invention.

When they met, Einstein was already a world famous physicist, thanks to his work on relativity, while Szilard was just starting out, as a graduate assistant at the University of Berlin. The impetus for the two men's collaboration on a refrigerator occurred in 1926, when newspapers reported the tragic death of an entire family in Berlin, due to toxic gas fumes that leaked throughout the house while they slept, the result of a broken refrigerator seal. Such leaks were occurring with alarming frequency as more people replaced traditional ice boxes with modern mechanical refrigerators which relied on poisonous gases like methyl chloride, ammonia, and sulfur dioxide as refrigerants. Einstein was deeply affected by the tragedy, and told Szilard that there must be a better design than the mechanical compressors and toxic gases used in the modern refrigerator. Together they set out to find one. They focused their attention on absorption refrigerators, in which a heat source–in that time, a natural gas flame–is used to drive the absorption process and release coolant from a chemical solution.

An earlier version of this technology had been introduced in 1922 by Swiss inventors, and Szilard found a way to improve on their design, drawing on his expertise in thermodynamics. His heat source drove a combination of gases and liquids through three interconnected circuits. One of the components they designed for their refrigerator was the Einstein-Szilard electromagnetic pump, which had no moving parts, relying instead on generating an electromagnetic field by running alternating current through coils. The field moved a liquid metal, and the metal, in turn, served as a piston and compressed a refrigerant. The rest of the process worked much like today's conventional refrigerators.

Einstein and Szilard needed an engineer to help them design a working prototype, and they found one in Albert Korodi, who first met Szilard when both were engineering students at the Budapest Technical University, and were neighbors and good friends when both later moved to Berlin. The German company A.E.G. agreed to develop the pump technology, and hired Korodi as a full-time engineer. But the device was noisy due to cavitation as the liquid metal passed through the pump. One contemporary researcher said it "howled like a jackal," although Korodi claimed it sounded more like rushing water. Korodi reduced the noise significantly by varying the voltage and increasing the number of coils in the pump. Another challenge was the choice of liquid metal. Mercury wasn't sufficiently conductive, so the pump used a potassium-sodium alloy instead, which required a special sealed system because it is so chemically reactive.

Despite filing more than 45 patent applications in six different countries, none of Einstein and Szilard's alternative designs for refrigerators ever became a consumer product, although several were licensed, thereby providing a tidy bit of extra income for the scientists over the years. And the Einstein/Szilard pump proved useful for cooling breeder reactors. The prototypes were not energy efficient, and the Great Depression hit many potential manufacturers hard. But it was the introduction of a new non-toxic refrigerant, freon, in 1930 that spelled doom for the Einstein/Szilard refrigerator. Interest in their designs has revived in recent years, fueled by environmental concerns over climate change and the impact of freon and other chlorofluorocarbons on the ozone layer, as well as the need to find alternative energy sources. In 2008, a team at Oxford University built a prototype as part of a project to develop more robust appliances, and a former graduate student at Georgia Tech, Andy Delano, also built a prototype of one of Einstein and Szilard's designs. Yet another team at Cambridge University is experimenting with cooling via magnetic fields. Perhaps this invention won't revolutionize the world, but in its own small way, it might help spare the planet–more than 70 years after Einstein and Szilard first conceived of it.

Prepared by: **Oday A. Hamadi**

Hasan Afifi[1]
Mohamad Abdel-Naby[2]
Said El-Hefnawie[1]
Aref Eliewa[1]
Ninet Ahmad[1]

[1] *National Research Center, Cairo, Egypt*
[2] *Department of Electrical Engineering, University of Qatar, P.O.Box 2713, Doha, QATAR*

Optical and Electrical Properties of Zinc Oxide Films Prepared by Spray Pyrolysis

The structural, optical and electrical properties of ZnO:In thin films prepared by spray pyrolysis method are examined. The used spray solution (0.2M) was prepared by adding indium chloride $InCl_3$ to the precursor of zinc acetate dissloved in mixed solution 80% H_2O: 20%CH_3OH. The XRD patterns for incorporated ZnO film with different concenteration of indium shows three addional peaks (100), (101) and (110) over the only one (002) appeared in pure ZnO. The intensities of these peaks are increased gradually with indium concentration while the (002) peak decrease to its minimum value at 3% In. The resistivity of ZnO films was improved by doping from $2.25x10^{2}$ Ω.cm for undoped to the minimum value at 2% doping concentration $2.6x10^{-2}$ Ω.cm. The optical bandgap of all films has no change by In addition and shows sharp absorption edge at 380nm.

Keywords: Optical properties, Electrical properties, Zinc oxide films, Spray pyrolysis
Received: 18 September 2010, **Revised**: 22 November, **Accepted**: 29 November 2010

1. Introduction

Zinc oxide (ZnO) is a well-known metal oxide semiconductor, which exhibits high transmittance as well as a change in conductivity from n-type to p-type based on doping [1–3]. ZnO was found with numerous technological applications such as window materials for solar cells, active material in sensors, high-density data storage devices, UV detectors, biodetectors, short-wavelength optoelectronic devices, etc [1]. The wide bandgap in the range between 3.2 eV and 3.8 eV with a large exciton binding energy of <60meV at room temperature is found stimulating the research interest since it can be used as an active material for the fabrication of the UV light-emitting diode (LED) and laser diode (LD), etc [4,5]. Similarly, ZnO is also interested to realize transparent thin film transistors (TFTs). Fabrication of the above-said devices requires obtaining properly doped n-type and p-type ZnO thin films to ensure proper carrier injection for device operation. Deposition of n-type ZnO is always favoured by non-stochiometric oxidation and inclusion of dopants such as Al [2,3]. So, it is quite easier to achieve low-resistive n-ZnO by most of the deposition methods such as MOCVD, MBE, PLD, sputtering, etc [1–5]. On the other hand, insulating-type ZnO (i-ZnO) needs to maintain better oxidation condition in order to avoid the formation of oxygen vacancy states ($V_o^{\cdot\cdot}$) of free electron contributors either by depositing at an ambient atmosphere or at excess oxygen pressure [6]. Whereas the deposition of p-type ZnO becomes tedious due to the major curdles arise from the presence of oxygen vacancy sites, lower acceptor solubility of a p-type dopant such as N, deep acceptor levels and net carrier compensation effects by native oxygen vacancy sites upon p-type doping [4–7]. So the attainment of p-type ZnO needs to overcome the existence of oxygen vacancy sites first and then enhance the dopant distribution [4]. Theoretical investigation suggests that the introduction of 'nitrogen' as a p-type dopant is more efficient than any other element, since it forms a N–Zn(O)–N complex and contributes excess 'holes' for conduction [8]. Generation of excess Zn is quite easier but the formation of the N–Zn(O)–N complex is not easy. So it is advisable to eliminate the oxygen vacancy sites and then try to obtain N-doping, which can prevent the loss of 'holes' upon net compensation. In this view, the vacuum processes such as MBE, MOCVD, CVD, sputtering, evaporation, etc, utilizes partial pressure of oxygen to maintain a better oxidation environment but still complete oxidation is rather difficult to achieve, and thus the N-doping become inefficient. Considering these facts, we selected spray pyrolysis and modified into pulsed-spray deposition in such a way that we can deposit films with lower deposition rates. This lower deposition rate is expected to oxidize the film into better stochiometric ratio and simultaneously dope the film with N due to the presence of N_2 as carrier gas.

Transparent conducting oxide (TCO) layers have been studied extensively because of their

broad range of application such as transparent electrodes in display [9] and in photovoltaic devices. [10] Among these TCO's, zinc oxide (ZnO) is a very promising candidate for future thin-film technology. Owing to their better stability in hydrogen plasma than that of tin oxide and indium tin oxide (ITO), which have been most used for transparent conducting electrodes, ZnO thin films are expected to be applied in the fabrication of hydrogenated amorphous silicon solar cells [11]. The additional advantages of zinc oxide films are the non-toxicity and the wide availability of its constituent raw materials. ZnO has a high transparency in the 0.4-2μm optical wavelength range, and it is a native n-type wide band gap semiconductor (E_g~3.3eV at room temperature), where its electrical conductivity is mainly due to oxygen vacancies or zinc excess at the interstitial position. Moreover, ZnO is attractive due to its large exciton binding energy of ~60meV. This large exciting binding energy provides excitonic emission more efficiently even at high temperature. Also, zinc oxide thin films with the *c*-axis orientation perpendicular to the substrate show piezoelectric properties and are useful in surface acoustic wave devices (SAW) and microelectromechanical systems (MEMS) [12]. Due to the various attractive properties for practical applications of ZnO, there have been much attention paid on the fabrication of ZnO films in recent years.

Zinc oxide (ZnO) is a wide-bandgap oxide semiconductor with a direct energy gap of about 3.37eV and a larger exciton binding energy (60meV), which assures more efficient exciton emissions at higher temperatures. The ZnO thin films have attracted significant attention as a wide gap semiconductor due to their wide range of electrical and optical properties. They have potential application in electronics, optoelectronics and information technology devices including displays, solar cells and sensors [13,14].

In the last decade, Zinc Oxide (ZnO) thin film attracts much interest due to valuable properties as it is high resistance to chemical attack, chemical stability and good adherence to many substrates. Also, ZnO possesses high optical transparent in the visible region and the index of refractive is ~1.8 enables them to act as a antireflection coating in solar cells applications. Its abundant in nature makes it a lower cost material when compared with ITO and SnO_2 materials.

Zinc oxide thin films have been prepared using various techniques, such as, DC magnetron sputtering [15], rf sputtering [16], evaporation [17], sol gel [18] and spray pyrolysis [19,20]. The spray pyrolysis is simple, inexpensive and suitable for large area coating. Pure ZnO thin films have extremely high electrical resistance which can be reduced by appropriate doping and heat treatment. The effect of substrate temperature and solvent were investigated previously [21]. In the present work the structure, optical and electrical properties of Indium doped ZnO films prepared by spray pyrolysis are examined.

2. Experiment

The ZnO thin films are deposited on microscope glass slices by spray pyrolysis. The doped ZnO thin films are prepared by adding indium chloride $InCl_3$ (1%, 2% and 3% by weight) to the precursor zinc acetate $Zn(CH_3CO_2).2H_2O$ dissolved in a mixed solution of 80% H_2O : 20% CH_3OH of 0.2 M. In our previous paper [21] studies depicted the role of the solvent on the characteristics of ZnO properties as well as the substrate temperature are found to be the mixture of 80% H_2O: 20% CH_3OH and substrate temperature 425°C for 30 min spray time are preferable to achieve ZnO films with structural, optical and electrical properties suitable for optoelectronic devices. The compressed air was used as a carrier gas with 20 L/min while the solution is feed to the designed glass nozzle by peristaltic pump to maintain the solution flow rate at 3 mL/min. The structure of the prepared ZnO thin films was detected using Pert-Philips x-ray diffraction with CuKα radiation (λ=1.5418 Å at 55 kV and 40 mA). The diffraction patterns were recorded automatically with scanning speed 2° per minute in the range (2θ=10-90°). The optical transmission studies were measured using double beam spectrophotometer, Model Jasco V-570.

3 Results and Discussions

3.1 Structural Properties

The obtained XRD patterns for pure and incorporated ZnO thin films with 1%, 2% and 3% indium by weight is shown in Fig. (1). The XRD patterns of all films are consistent with the pattern of ZnO powder reported in standard JCPDS data file. The lattice constants of these films are calculated from the obtained values of d-spacing and their corresponding (*hkl*). The values of the lattice constants are found to be (a=3.24Å and C=5.19Å) which are close to the standard value of hexagonal form of ZnO powder. The pure ZnO thin films show only one characteristic peak at 2θ=34.46° which corresponds to (002) nearly like that prepared by epitaxy technique. The addition of In doesn't affect the main peaks position which reflect the existence of ZnO single phase. Three other principal peaks (100), (101) and (110) are appeared by indium incorporating. The

intensities of these planes are increased gradually by incorporating In with percentage 1% and 2%. In contrast the film incorporated with 3%., these intensities of the peaks are decreased, while the principal plane (002) appeared in the pure ZnO films reduce to its minimum intensity. The crystallite size of ZnO films is calculated using Scherrer formula:

$$D = 0.94\,\lambda / \Delta(2\theta)\cos\theta \qquad (1)$$

where D is the mean grain size, $\Delta(2\theta)$ is the full width at half maximum of the diffraction line in radius, θ is the diffraction angle and λ is the wave length of X-ray (1542Å). The grain size is listed in Table (1)

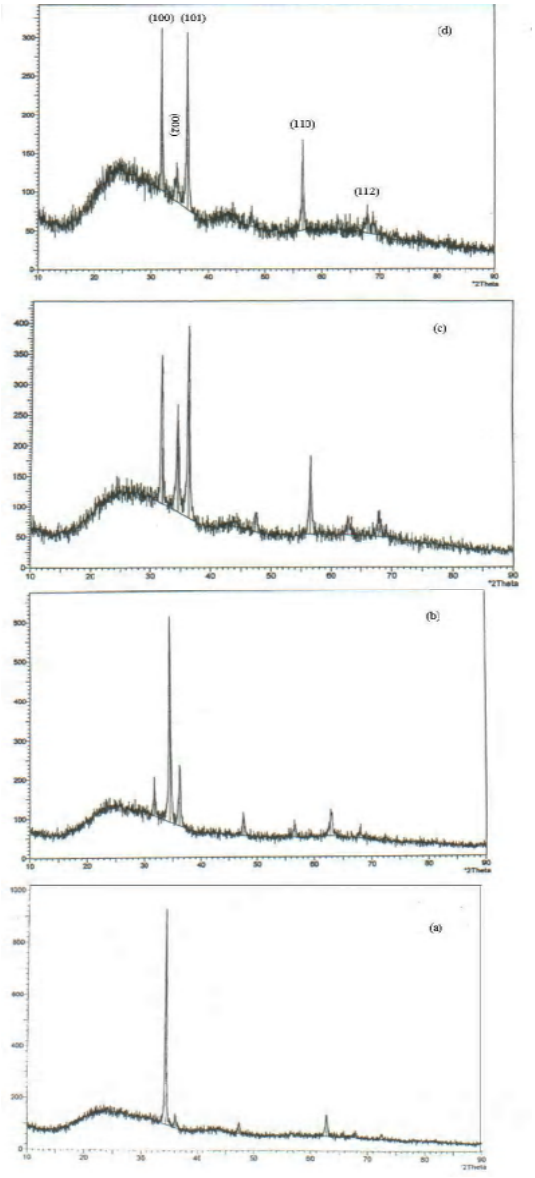

Fig. (1) XRD patterns for pure and doped ZnO thin films (a) pure ZnO, (b), 1% In, (c) 2% In, (d) 3% In

Table (1) The mean grain size of ZnO films versus dopant concentration

Dopant	Grain size (nm)	
	(100)	(101)
1%	44	57
2%	60	40
3%	37	38

3.1.1 EDX

The film composition of indium doped zinc oxide was determined using energy dispersive of x-ray (EDX) using SEM model Philips XL30 attached with EDX unit with accelerating voltage 30kV. It is used to estimate the elements ratios exist in the prepared films. Figure (2) shows the EDX corresponding to ZnO incorporated with 2% and 3%, respectively. The appeared two principal peaks are related to Zn and In elements in the film while the other peaks are related to the elements of glass substrate.

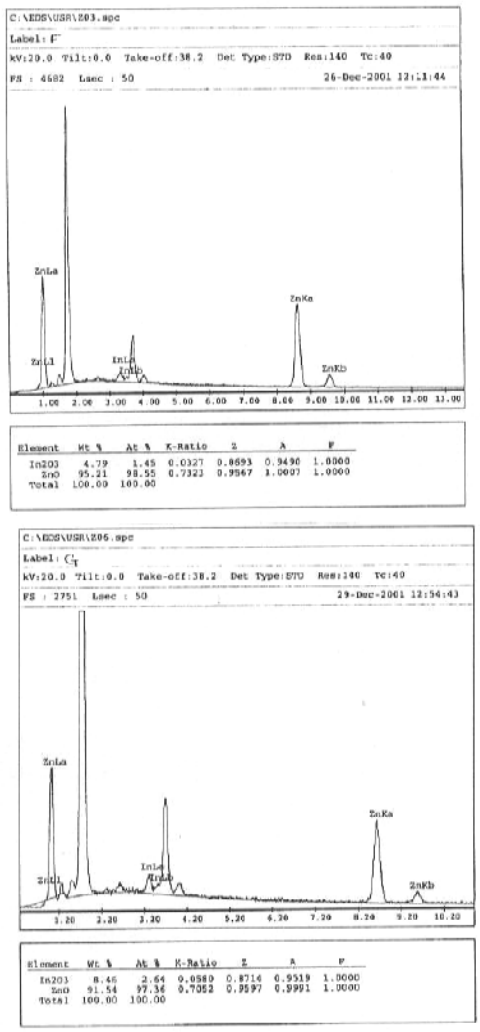

Fig. (2) EDX of ZnO films incorporated by indium (a) 2% In, (b) 3% In

ISSN 1813-2065

3.2 Optical Properties

The transmittance versus wavelength for pure and doped ZnO thin films is shown in Fig. (3). It is observed that the films are highly transparent with sharp absorption edge at λ=380nm. The optical bandgap values are obtained from the plot $(\alpha h\nu)^2$ *vs. hν* by extrapolating the linear portion of the plot to $(\alpha h\nu)^2=0$.

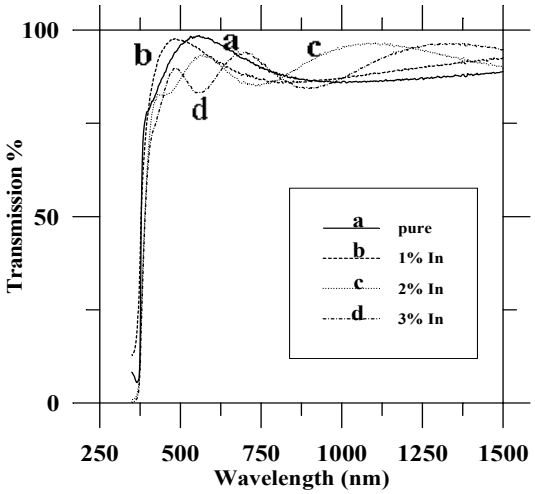

Fig. (3) The transmittance of pure and doped ZnO thin films versus wavelength

Figure (4) shows the optical bandgap for pure and doped ZnO thin films. The calculated optical band gap has no change by indium addition; its value is 3.26 e.V.

Figure (5) shows the variation of absorption coefficient α with wavelength for undoped and doped ZnO films. It is clear that the absorption coefficient is sharply decreased near the band edge indicating the good crystallinity.

In the visible region, the absorption coefficient increase with the doping concentration. The refractive index n calculated from transmittance for undoped and doped ZnO thin films are shown Fig. (6). The refractive index varies from 1.7~2 in the visible range which are preferred for antireflection coating materials.

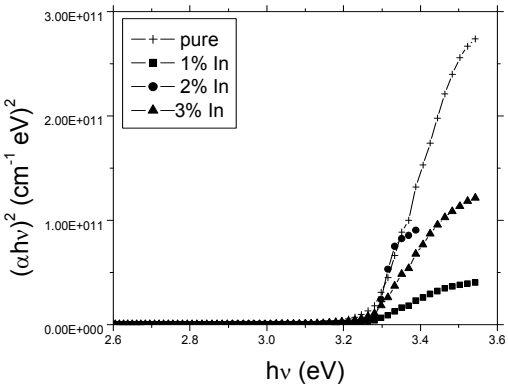

Fig. (4) Plot of (αhv) 2 vs. hv for pure and doped ZnO

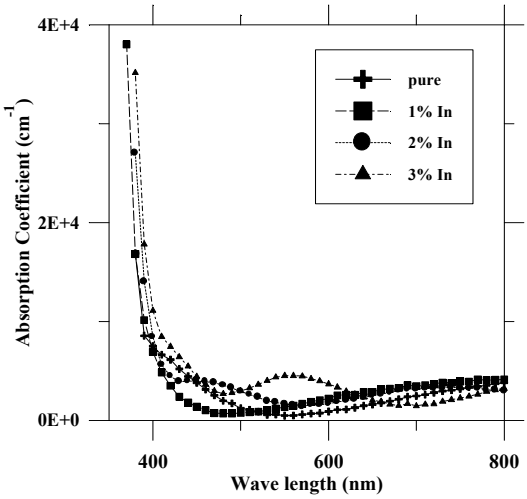

Fig. (5) The variation of absorption coefficient α versus wave length for pure and doped ZnO films

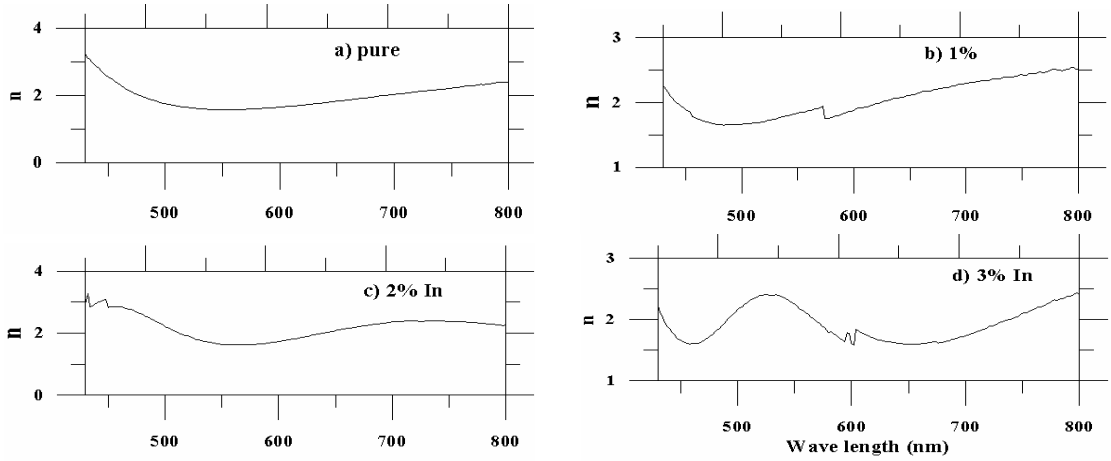

Fig. (6) The refractive index (n) versus wavelength

3.3 Electrical Properties

Pure ZnO thin films have extremely high electrical resistivity. Indium incorporation shows drastic reduces in the resistivity value (`four orders of magnitude). The pure ZnO films have resistivity value $2.25x10^{2}$ Ω.cm while the incorporated film with 2% doping concentration have a minimum value $2.6x10^{-2}$ Ω.cm. The variation of electrical resistivity with the dopant concentration is shown in Fig. (7).

3.4 Figure of Merit

We deposited ZnO: In thin film as oxide semiconductor window layer on single crystal silicon to form solar cell, the results will be published later. Figure of merit Φ is useful to determine the films which have less absorption and good conductivity to reduce the series resistance. It is calculated using the following formula [22]:

$$\Phi = 1/\alpha\rho \quad (2)$$

The calculated values for pure and ZnO that incorporated with different ratios of indium are listed in Table (2). It is clear that the ZnO film incorporated with 2% indium concentration gives the higher value of figure of merit ($2.1x10^{-3}$S). This related to the high reduction in electrical resistivity and good crystallinity that it is given in Fig. (1).

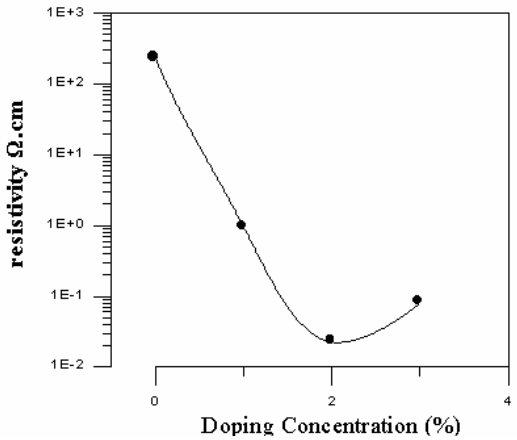

Fig. (7) The effect of doping on the resistivity

Table (2) The figure of merit for pure and doped ZnO thin films

Doing Concentration	Absorption coeff. α x10^{3} at λ= 500nm (cm^{-1})	Resist. ρ (Ω.cm)	Figure of Merit ϕ(S)
Pure	1.237	$2.25x10^{2}$	$3.59x10^{-6}$
1%	0.744	$6.47x10^{-1}$	$2.1x10^{-3}$
2%	2.976	$2.6x10^{-2}$	$1.3x10^{-2}$
3%	2.922	$7.36x10^{-2}$	$4.6x10^{-3}$

4. Conclusions

It is clear that the addition of indium as a dopant shows an additional peaks (100), (101) and (110) over the only one (002) appeared in pure ZnO films. Also the optical band gap of ZnO films hasn't changed by indium addition and shows sharp absorption edge at 380 nm. The ZnO film incorporated with 2% In gives a higher figure of merit ($2.1x10^{-3}$S) due to its larger reduction in electrical resistivity ($2.6x10^{-2}$ Ω.cm). The absorption coefficient in the visible region increases with the doping concentration.

References

[1] R.J. Honga et al., *J. Cryst. Growth* 249 (2003) 461–469.
[2] Y. Marfaing and A. Lusson, *Superlattices Microstruct.* 38 (2005) 385–396.
[3] T.H. Vlasenflin and M. Tanaka, *Solid State Commun.*, 141 (2007) 292–294.
[4] K. Wang, Y. Vygraneko and A. Nathan, *Thin Solid Films,* 515 (2007) 6981–6985.
[5] S.K. Hazra and S. Basu, *Sensors Actuators,* B117 (2006) 117–182
[6] A.V. Singh and R.M. Mehra, *J. Appl. Phys.,* 93 (2003) 396–398.
[7] M.A. Kaid and A. Ashour, *Appl. Surf. Sci.,* 253 (2007) 3029–3033.
[8] K. Minegishi et al., *Japan. J. Appl. Phys.,* 2(36) (1997) L1453.
[9] C. Guillén and J. Herrero, *Thin Solid Films,* 480–481 (2005) 129.
[10] M. Emziane et al., *Thin Solid Films*, 480–481 (2005) 377.
[11] D. Rajesha, J. Tapatia and R. Swatia, *Solar Ener. Mater. Solar Cells*, 86 (2005) 207–216.
[12] P.B. Kirby et al., *J. Europ. Ceram. Soc.*, 23 (2003) 2689.
[13] S. Bandyopadhyay, G.K. Paul, S.K. Sen, *Solar Ener. Mater. Sol. Cells* 71 (2002) 103.
[14] Y. Natsume and H. Sakata, *Thin Solid Films*, 372 (2000) 30.

[15] S. Brehme et al., 13th *European Photovoltaic Solar Energy Conf.*, (1995) 23-27.
[16] T.L. Yang et al., *Thin Solid Films,* 326 (1998) 60-62.
[17] J. Ma et al., *Thin Solid Films,* 279 (1996) 213-215.
[18] W. Tang and D.C. Cameron, *Thin Solid Films*, 238 (1994) 83-87.
[19] C. Messaoudi, D. Sayah and M. Abd-Lefdii, *phys. stat. sol. a*, 151 (1995) 93-97.
[20] J. Benny et al., *Mater. Chem. and Phys.,* 58 (1999) 71-77.
[21] H. Afifi et al., "Solvent Effect On Physical Properties Of Zinc Oxide Films Prepared By Spray Pyrolysis", World Renewable Energy Congress VII (2002) Cologne, Germany.
[22] P. Nunes, E. Fortunato and R. Martines, *Thin Solid Films,* 383 (2001) 277-280.

This article was reviewed at Department of Electronic and Electrical Engineering, National Technical University, Seoul, KOREA, and School of Applied Sciences, University of Technology, Baghdad, IRAQ

Iraqi Journal of Applied Physics
Subject Index 2005-2010

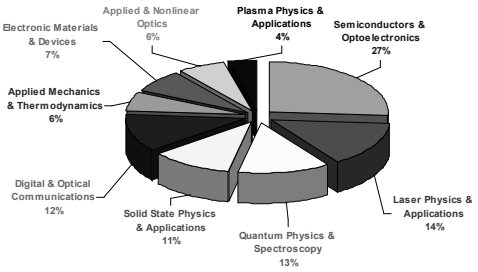

Articles published in IJAP (2005-2010) by subject

Applied & Nonlinear Optics

- Curvelet-Based Optical Flow Estimation Algorithm Based on Central Derivatives, 6(2), 13
- Design of a Multi-Electrode Immersion Lens for Ion-Optical Systems, 2(1,2), 27
- Investigations of Linear and Nonlinear Optical Properties of Transparent ZnO Thin Films Grown by Sol-Gel Method, 6(3), 29
- Key Mechanisms of the Nonlinear Amplification: Physics and Applications, 1(2), 3
- New Method for Calculating Cumulative Line Energy Using Pupil Function Technique, 2(1,2), 7
- Some Optical Properties of an Electrostatic Immersion Lens Using the Charge Density Method, 1(4), 21
- Temperature-Dependent Birefringence Properties of $Be_3Al_2Si_6O_{18}$ Crystal, L2(1), 12

Applied Mechanics & Thermodynamics

- Characterization of D.C. Sputtering System, L1(1), 3
- Employing Inner Triplet Upgrade in Cold Mass Cooling Design for Large Hadron Collider, L2(1), 19
- HAZ Extent Analysis in Fiber-Reinforced Plastic Grooving by Laser, 1(1), 3
- Optimization Of Composition, Structure and Characteristics of Metal in Arc Deposition, 5(2), 37
- Marangoni Convection Effect on the Melting of GaSb/InSb/GaSb Sandwich Structured Sample, 4(2), 35
- Modeling of the Preheating Effect on Keyhole Laser Welding Efficiency, L1(1), 10
- Using Longitudinal Surface Acoustic Waves for Non-Destructive Testing of Inner Surfaces, L1(2), 9
- Torque and Magnetic Flux Analysis Using an Advanced Dynamic Dynamometer Test Bed for Electromechanical Motors, 5(1), 13

Digital & Optical Communications

- A CPW-Fed Printed Monopole Ultra-Wideband Antenna with E-Shaped Notched Band Slot, 6(4), 17
- A New Fractal Microstrip Bandpass Filter Design Based on Dual-Mode Square Ring Resonator for Wireless Communication Systems, 5(1), 7
- Analysis and Design of Combined Fractal Dipole Wire Antenna, 5(2), 29
- Classification of Digital Modulation Using Wavelet Transform, 1(3), 15
- Coherent Detection in Optical Fiber Systems, 3(1), 3
- Comparative Evaluation of Bit Error Rate in Frequency Selective Fading Channels Employed in Wavelet Modulation, L1(2), 14
- Design and Analysis of Special Small Size Cross Dipole Antenna, 6(2), 19
- Determination of The Satellite Images Orientation Using DCT Coefficients, 6(2), 31
- Effect of Chirping on Received Pulse Shape in Optical Fiber Communications, L2(2), 7
- Linear Adaptive Antenna Array Geometry Effects on Radiation Pattern, L3(1), 3
- Phase Noise Compensation for Coherent Orthogonal Frequency Division Multiplexing in Optical Fiber Communications Systems, 5(2), 3
- Quantum Limit Characterization of Signal-to-Noise Ratio using Phase-Shift Keying in Homodyne Detection, L3(1), 11
- Range-Coverage Extension Using Smart Antennas in Mobile Communications Systems, 5(2), 25
- Signal Mechanism Analysis of Fiber Arrival Time in Fiber Optic Pin, 5(2), 13
- Synchronization Scheme for Secured Communications System Based on Chaotic Signals, L3(1), 7
- Transmission of Compressed Video Signals through Spread Spectrum Channel, 6(4), 9

Electronic Materials & Devices

- Characterization of E-Mode InZnO Thin Film Transistors Produced by DC Sputtering Technique, L3(1), 19
- Electrical Properties of Cu_2O Films Prepared by Electro-Deposition Method, L1(2), 27
- Extraction of Doping Profile in Substrate of MNOS capacitor Using Fast Voltage Ramp Deep Depletion C-V method, 6(1), 35
- Fabrication and Characterization of InZnO TFTs Grown on Transparent Conductive Oxide Substrate by DC Sputtering Technique, 6(1), 41
- Field Dependent Critical Trap Density for Thin Gate Oxide Breakdown, 6(3), 15
- Junction Characteristics of Wide-Emitter (p)CdS-(n)Si-(p)Si Heterojunction Transistor, 2(1,2), 3
- New High Angular Resolution Detection System for Direction Recognition, 1(3), 27
- Performance Comparison of InP-Based Phototransistors to PIN and UTC Photodiodes, 4(4), 13
- Recent Developments in Silicon Photomultipliers, 4(3), 27

ISSN 1813-2065

Laser Physics & Applications

Plasma Physics & Applications

Quantum Physics & Spectroscopy

Semiconductors & Optoelectronics

Solid State Physics & Applications

* * *

* * *

ISSN 1813-2065

Iraqi Journal of Applied Physics
Author Index 2005-2010

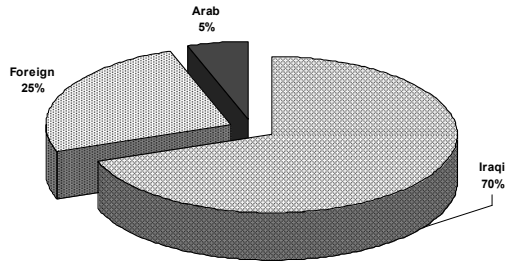

Authors of IJAP articles by nationality

ISSN 1813-2065

THE IRAQI JOURNAL OF APPLIED PHYSICS
EDITORIAL BOARD

COPYRIGHT RELEASE
Iraqi Journal of Applied Physics (IJAP)

We, the undersigned, the author/authors of the article titled
……
……
……
……
……
……
that is presented to the Iraqi Journal of Applied Physics (IJAP) for publication, declare that we have neither taken part or full text from any published work by others, nor presented or published it elsewhere in any other journal. We also declare transferring copyrights and conduct of this article to the Iraqi Journal of Applied Physics (IJAP) after accepting it for publication.

The authors will keep the following rights:
1. Possession of the article such as patent rights.
2. Free of charge use of the article or part of it in any future work by the authors such as books and lecture notes without referring to the IJAP.
3. Republishing the article for any personal purposes of the authors after taking journal permission.

To be signed by all authors:

Signature:……..date: ……

Printed name: ……

Signature:……..date: ……

Printed name: ……

Signature:……..date: ……

Printed name: ……

Correspondence address:……...
……..
Address:……
……
……
Telephone:……..email: ……..

Note: Please complete and sign this form and mail it to the below address with your manuscript

The Iraqi Journal of Applied Physics
P. O. Box 55259, Baghdad 12001, IRAQ
Website: www.ijap.org
Email: editor@ijap.org
Phone: +964 7901274190

IRAQI JOURNAL OF APPLIED PHYSICS

CONTENTS

